Universitat de les Illes Balears

BACHELOR'S THESIS

MAGNETOHYDRODINAMIC WAVES INSIDE THE SUN

Jaume Llabrés Rubio

Degree in Physics

Faculty of Science

Academic Year 2020-21

MAGNETOHYDRODINAMIC WAVES INSIDE THE SUN

Jaume Llabrés Rubio

Bachelor's Thesis

Faculty of Physics

University of the Balearic Islands

Academic Year 2020-21

Key words:

Complex Empirical Orthogonal Function Analysis, Waves, Hydrodynamic simulations of the solar tachocline, Rossby waves

Thesis Supervisor's Name Ramon Julio Oliver Herrero

Tutor's Name (if applicable)

Abstract

In this work, the complex empirical orthogonal function (CEOF) method is used to analyse a numerical simulation of the tachocline. This method extracts information on the waves contained in a two-dimensional field and provides this knowledge in the form of four CEOF functions or measures. Firstly, we construct one- and two-dimensional synthetic signals made of the sum of standing and propagating waves to help interpret the CEOF functions. The CEOF analysis is able to identify each wave component of the field. Also, the amplitude, frequency and wavenumbers are recovered with outstanding accuracy. After testing the method we are able to apply the CEOF analysis to three scalar variables that come from a hydrodynamic numerical simulation of the tachocline: the perturbation of the tachocline thickness, h, and the longitudinal and latitudinal velocity components, u and v. Two physical modes of oscillation present in all variables are found. In addition to the amplitudes of the three variables, their wavenumbers and the frequency, the spatial distribution of h, u and v is also determined. Moreover, the CEOF method also allows to recover some properties of the tachocline differential rotation and reveals the presence of non-linear waves in the numerical simulation.

Contents

1 Introduction **1**

2 Complex Empirical Orthogonal Function method **2**
2.1 Algorithm . . . 2
2.2 Interpretation . . . 3

3 Tests with synthetic signals **5**
3.1 One-dimensional waves . . . 5
3.2 Two-dimensional waves . . . 8
3.2.1 Synthetic field . . . 8
3.2.2 CEOF analysis . . . 9
3.3 Two-dimensional waves with noise . . . 13

4 Oscillations in the solar tachocline **16**
4.1 Introduction . . . 16
4.2 Frequencies and wavenumbers . . . 18
4.3 CEOF results . . . 18
4.3.1 Tachocline differential rotation . . . 18
4.3.2 Wave with frequency near 0.21 . . . 20
4.3.3 Wave with frequency near 0.47 . . . 23
4.3.4 Wave with frequency near 0.22 . . . 25
4.4 Conclusions . . . 26

5 Discussion and future work **28**
5.1 Discussion . . . 28
5.2 Future work . . . 29

Chapter 1

Introduction

The Complex Empirical Orthogonal Function (CEOF) analysis uses as input a scalar field (e.g. the pressure, a velocity component of a fluid, etc.) whose values on a spatial grid are known for some discrete time values. Its output is knowledge about the amplitude, frequency and wavenumber of waves present in the scalar field. The CEOF analysis makes use of the Hilbert transform to create the analitic signal of the input field, which is then used to construct its zero lag covariance matrix. This matrix is diagonalised and its eigenvectors are inspected to reveal the properties of waves in the scalar field. It can be seen that the CEOF method is completely empirical and the obtained eigenfunctions are orthogonal by construction, hence its name.

The CEOF analysis was introduced by Barnett (1983), who explains that Wallace & Dickinson (1972), Rasmusson et al. (1981) and Anderson (1982) dealt with ideas that form the basis of the CEOF method, but did not provide a formal development of the method as in Barnett (1983). Moreover, in this last work it is shown that the CEOF analysis provides more information on the waves present in a scalar field than discussed in the previous papers. Barnett (1983) was concerned with propagating waves, but, as we will show in this thesis, the CEOF method is equally qualified to extract the parameters of standing waves contained in the scalar field.

Terradas et al. (2004) made an application of the CEOF analysis to the intensity of a coronal loop in the 171 Å passband. In this paper an introduction to the CEOF method is also given by means of a two-dimensional synthetic field that contains a standing and a propagating wave. Here we follow this idea and provide an explanation of the CEOF functions that result from the application of the CEOF method and clarify their interpretation based on very simple one- and two-dimensional synthetic signals made of the sum of several waves. In the one-dimensional case a propagating and a standing pattern are summed. In the two-dimensional case, a wave that propagates in the two directions, a standing wave in the two directions and a wave that propagates in one direction and is a standing one in the other are summed. We show that, thanks to the simplicity of these constituting waves, their amplitude, frequency and wavenumber can be retrieved with extraordinary accuracy.

We also analyse the results of a hydrodynamic numerical simulation of Dikpati (2012) and Dikpati et al. (2017), who studied the non-linear hydrodynamic evolution of a thin layer of the Sun called the tachocline. These authors studied the energy interchange between unstable Rossby waves and the tachocline differential rotation. Our purpose can be expressed as this question: is it possible to obtain, with the help of the CEOF analysis, detailed information about the physical modes of oscillation that form the basis of the energy interchange between Rossby waves and differential rotation?

This thesis is organised as follows: in Chapter 2 we present a description of the CEOF method. Chapter 3 is devoted to presenting the application of this method to some synthetic signals with the aim of understanding the output of the CEOF analysis. The results of a numerical simulation used in Dikpati (2012) and Dikpati et al. (2017) are analysed in Chapter 4. The conclusions are summarised in Chapter 5, where some ideas for future work are also given.

Chapter 2

Complex Empirical Orthogonal Function method

2.1 Algorithm

In this section we describe the CEOF method and for this purpose we follow Barnett (1983). We are only concerned about the algorithm to make the CEOF analysis of a signal. For a more detailed account of the CEOF method the reader is referred to the previous reference.

Let us consider a two-dimensional scalar field, $V(\vec{r},t)$, measured on a quadrilateral mesh with $N_x \times N_y$ discrete points. Every mesh location is defined by a couple of values, $\vec{r}_k = (x_i, y_j)$, where $i = 1,2,...,N_x$, $j = 1,2,...,N_y$, $k = 1,2,...,N_{xy}$. The parameter $N_{xy} = N_x N_y$ is the number of points of our grid. In addition, time is discretised on a set of N_t equally spaced values, t_l, with $l = 1,2,\ldots,N_t$. Hence, the discretised field is a cube with $N_x \times N_y \times N_t$ values and hereafter is represented by $V(\vec{r_j},t_l)$. In this work we use the indices i and j for the two spatial positions on the grid, the index k for the corresponding position vector and the index l for time.

If $V(\vec{r}_k,t_l)$ is both simply and square integrable at each spatial position $\vec{r}_k$, then at every $\vec{r}_k$ it can be expressed as an infinite sum of sine waves, known as a Fourier series:

$$V(\vec{r}_k,t_l) = \sum_{\omega} a_k(\omega)\cos(\omega t_l) + b_k(\omega)\sin(\omega t_l), \tag{2.1}$$

where only positive frequencies are needed. Each Fourier mode is characterised by its frequency ω, related with the period of the wave by $\omega = 2\pi/T$, and is weighed by the Fourier coefficients $a(\omega)$ and $b(\omega)$ defined in the usual way. Equation (2.1) can also be written in terms of a complex representation. This form is more suitable because the time domain contains crucial information on traveling features present in the scalar field:

$$U(\vec{r}_k,t_l) = \sum_{\omega} c_k(\omega)\, e^{-i\omega t_l}, \tag{2.2}$$

where $c(\omega) = a(\omega) + ib(\omega)$. Barnett (1983) shows that expanding the exponential in the latter expression it becomes:

$$U(\vec{r}_k,t_l) = V(\vec{r}_k,t_l) + i\hat{V}(\vec{r}_k,t_l), \tag{2.3}$$

where the $\hat{}$ symbol represents the Hilbert transform of a signal. Thus, $U(\vec{r}_k,t_l)$ is the analitic signal of $V(\vec{r}_k,t_l)$.

The next step is to calculate the elements of the zero lag covariance matrix, C, as

$$C_{kk'} = \frac{\sum_{l=1}^{N_t} U^*(\vec{r}_k,t_l)\,U(\vec{r}_{k'},t_l)}{N_t}, \tag{2.4}$$

where * denotes complex conjugation. The $C_{kk'}$ element gives a measure of the spectral variability of the field between the kth and the k'th locations. By construction C is a Hermitian matrix, i.e. it is a square matrix that is equal to its own conjugate transpose. Since the size of this matrix is N_{xy}, its diagonalisation yields N_{xy} real and non-negative eigenvalues, λ_n, and their corresponding complex eigenvectors, $E_n(\vec{r}_k)$, with $n = 1, 2, \ldots, N_{xy}$. Next we describe how the pair $\{\lambda_n, E_n(\vec{r}_k)\}$ can be used to build a "CEOF mode", which may or may not correspond to a physical wave or oscillation. This will become clear in our two-dimensional test with noise (see Section 3.3).

First, the time evolution of the CEOF mode can be obtained by projecting the field $U(\vec{r}_k, t_l)$ onto each eigenvector $E_n(\vec{r}_k)$ and summing over all positions:

$$A_n(t_l) = \sum_{k=1}^{N_{xy}} U(\vec{r}_k, t_l)\, E_n(\vec{r}_k). \tag{2.5}$$

By definition, the nth CEOF mode, $U_n(\vec{r}_k, t_l)$, involves a spatial part, the eigenvector $E_n(\vec{r}_k)$, and the temporal part $A_n(t)$:

$$U_n(\vec{r}_k, t_l) = E_n^*(\vec{r}_k)\, A_n(t_l)\,. \tag{2.6}$$

The product $E_n^*(\vec{r}_k)\, A_n(t_l)$ conforms a representative oscillatory mode present in the field. The spatial and temporal variation of the nth CEOF mode can be obtained by taking the real part of this product. Therefore, the original field $U(\vec{r}_k, t_l)$ can be reconstructed by summing over all the modes

$$U(\vec{r}_k, t_l) = \mathrm{Re}\left[\sum_{n=1}^{N_{xy}} E_n^*(\vec{r}_k) A_n(t_l)\right], \tag{2.7}$$

where Re denotes the real part.

Finally the contribution of the nth mode to the total field variance can be quantified by:

$$\frac{\lambda_n}{\sum_{n=1}^{N_{xy}} \lambda_n}. \tag{2.8}$$

According to the latter expression, the most dominant modes in the field V will have the largest eigenvalues.

2.2 Interpretation

Each CEOF mode can be described by four measures or CEOF functions that determine possible moving or standing wave features in the field. They are empirical in the sense that they come from the diagonalisation of the zero lag covariance matrix.

1. Spatial amplitude function. This function shows the spatial distribution of variability associated with each eigenmode. It gives a measure of the spatial homogeneity, for each mode, in the magnitude of the field. Its definition for the nth CEOF mode is:

$$S_n(\vec{r}_k) = \left[E_n(\vec{r}_k)\, E_n^*(\vec{r}_k)\right]^{1/2}. \tag{2.9}$$

2. Spatial phase function. The relative phase fluctuation among different spatial positions of the domain is exhibited in this measure. It oscillates between $-\pi$ and π. The spatial phase associated to the nth CEOF mode is:

$$\Theta_n(\vec{r}_k) = \arctan\left[\frac{\mathrm{Im}\left(E_n(\vec{r}_k)\right)}{\mathrm{Re}\left(E_n(\vec{r}_k)\right)}\right], \tag{2.10}$$

where Im designates the imaginary part.

3. Temporal amplitude function. This is a measure of temporal variability in the amplitude of a CEOF mode and for the nth one is:

$$R_n\left(t_l\right) = \left[A_n\left(t_l\right) A_n^*\left(t_l\right)\right]^{1/2}. \tag{2.11}$$

4. Temporal phase function. This function gives the temporal variation of the phase related with the field. It is defined by:

$$\Phi_n\left(t_l\right) = \arctan\left[\frac{\mathrm{Im}\left(A_n\left(t_l\right)\right)}{\mathrm{Re}\left(A_n\left(t_l\right)\right)}\right]. \tag{2.12}$$

   As the spatial phase, it also fluctuates between $-\pi$ and π.

These four definitions allow us to express the spatial and the temporal part $E_n\left(\vec{r}_k\right)$ and $A_n(t_l)$ of each CEOF mode in exponential form:

$$E_n\left(\vec{r}_k\right) = S_n(\vec{r}_k)e^{i\Theta(\vec{r}_k)}, \tag{2.13}$$

$$A_n\left(t_l\right) = R_n(t_l)e^{i\Phi(t_l)}. \tag{2.14}$$

Now Equation (2.6) reads:

$$U_n\left(\vec{r}_k, t_l\right) = \mathrm{Re}\left\{R_n(t_l)S_n(\vec{r}_k)e^{i[\Phi_n(t_l)-\Theta_n(\vec{r}_k)]}\right\}, \tag{2.15}$$

where we have explicitly written that the real part of this expression will be used.

To clarify the interpretation of these measures the next chapter is devoted to present some simple examples of the CEOF analysis of synthetic one- and two-dimensional fields.

We have written a Python implementation of the algorithm explained in this section. This implies computing the analitic function of $V(\vec{r}_k, t_l)$ (Equation (2.3)), the zero-lag covariance matrix (Equation (2.4)), its eigenvalues and eigenvectors (λ_n and $E_n(\vec{r}_k)$) and the projection of Equation (2.5). At this point we are ready to obtain, for each CEOF mode, the four measures of Equations (2.9)–(2.12) and the reconstruction of Equation (2.15).

Chapter 3

Tests with synthetic signals

This section consists of two parts. In the first one, one-dimensional waves have been studied to understand how the CEOF method works and what the CEOF functions represent. In the second part, the complexity of the waves will be increased by adding one dimension to the spatial part. After this study, we will be able to analyse numerical simulations containing actual tachocline waves.

3.1 One-dimensional waves

Before starting to study two-dimensional waves, it is interesting to understand the behaviour of the four CEOF measures in the one-dimensional case. Considering standing or propagating waves in the x-direction, the position vector $\vec{r}_k$ becomes x_i and now only one index is necessary to define a location on the mesh. This case is equivalent to that of a mesh with $N_y = 1$. So, the number of points of the surviving dimension hold all the spatial locations. In the one-dimensional case Equation (2.15) can be written as:

$$U_n(x,t) = \mathrm{Re}\left\{R_n(t)S_n(x)e^{i[\Phi_n(t)-\Theta_n(x)]}\right\}, \tag{3.1}$$

where for simplicity we have omitted the subscripts i and l in x_i and t_l. The subscript n tells us that we are dealing with the nth CEOF mode.

Let us construct a field equal to the sum of the two simplest linear waves in one dimension. The first is the most elementary one: a propagating wave with constant amplitude A_p, wavenumber k_p and frequency ω_p:

$$W_p(x,t) = A_p \cos(\omega_p t - k_p x). \tag{3.2}$$

The second one corresponds to a wave which oscillates in time but does not propagate in space, i.e. it is a standing wave. Its amplitude, wavenumber and frequency are A_s, k_s and ω_s, respectively:

$$W_s(x,t) = A_s \cos(k_s x)\cos(\omega_s t). \tag{3.3}$$

The subscripts p and s indicate whether the wave is propagating or standing.

Finally, our one-dimensional field is defined as:

$$V(x,t) = W_p(x,t) + W_s(x,t), \tag{3.4}$$

where the numerical parameters of the waves are shown in Table 3.1.

Now we consider $N_x = 90$, $N_y = 1$ and $N_t = 120$, so a $90 \times 1 \times 120$ data cube is built as the CEOF input. The number of CEOF modes retrieved after the diagonalisation of the covariance matrix is equal to $N_{xy} = 90$, but only two of them have some meaning as actual waves. These two CEOF modes contain 99.99% of the variance of the field of Equation (3.4); see the last line

	Input data		CEOF results	
Wave type	Standing wave	Propagating wave	Standing wave	Propagating wave
A	2.378	1.457	2.383	1.456
k	0.942	1.257	0.932	1.256
ω	8.378	3.142	8.375	3.140
Mode variance			57.59%	42.40%

Table 3.1: Test of the CEOF method with one-dimensional synthetic data. The 2nd and 3rd columns give the wave parameters used in Equation (3.4). Arbitrary units are considered. The 4th and 5th columns provide the same parameters calculated from the CEOF analysis. The last row contains the percentage of the variance contributed by each CEOF mode.

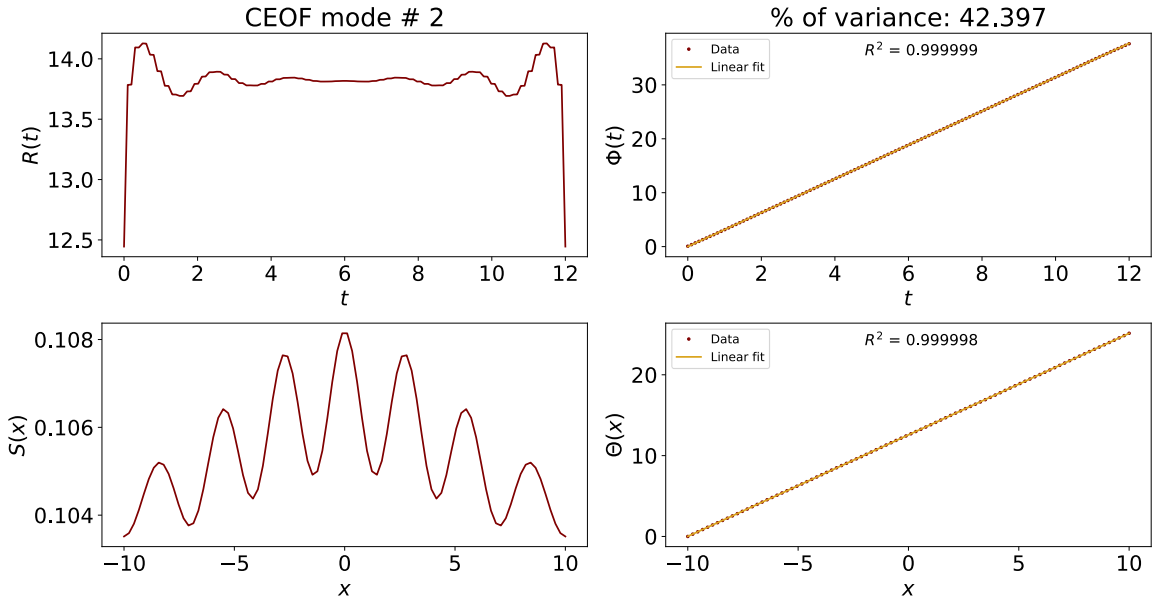

Figure 3.1: Second CEOF mode of the one-dimensional test, corresponding to the propagating wave. The four CEOF measures defined by Equations (2.9)–(2.12) are plotted.

of Table 3.1. The four measures defined in Section 2.2 are shown for these two modes in Figures 3.1 and 3.2.

We start the discussion of these results with the second CEOF mode, that contains 42.40% of the variance of the field and turns out to represent the propagating wave, as we will see. To stress the similarities between Equations (3.1) and (3.2) we write the last one as:

$$W_p(x,t) = \mathrm{Re}\left[A_p e^{i(\omega_p t - k_p x)}\right]. \tag{3.5}$$

From the comparison of the complex exponential in Equations (3.1) and (3.5), we expect the temporal (spatial) phase of the CEOF mode to be linear in t (or x) with a slope ω_p (or k_p). Because they are computed with Equations (2.10) and (2.12), both CEOF measures lie in the range $[-\pi, \pi]$ and consequently have a sawtooth wave shape. Taking into account that both phases are angles in a complex exponential, they are unwrapped. This means that the independent variable (i.e. t or x) is gradually increased until a phase jump of $+2\pi$ or -2π is detected. At this point, all values of the phase for larger values of the independent variable are decreased or increased by 2π, respectively, and the process of finding new phase jumps of $+2\pi$ or -2π is repeated to the right of this position. After this phase unwrapping, the temporal and spatial

phases are transformed from a sawtooth profile into a ramp: see the right panels of Figure 3.1. The square of the Pearson correlation coefficient, R^2, displayed in these two panels, indicates an almost perfect linear behaviour. The slopes of $\Phi(t)$ and $\Theta(x)$, which are obtained by means of a linear least-squares fit, provide excellent approximations to the frequency and wavenumber of the propagating wave: see Table 3.1.

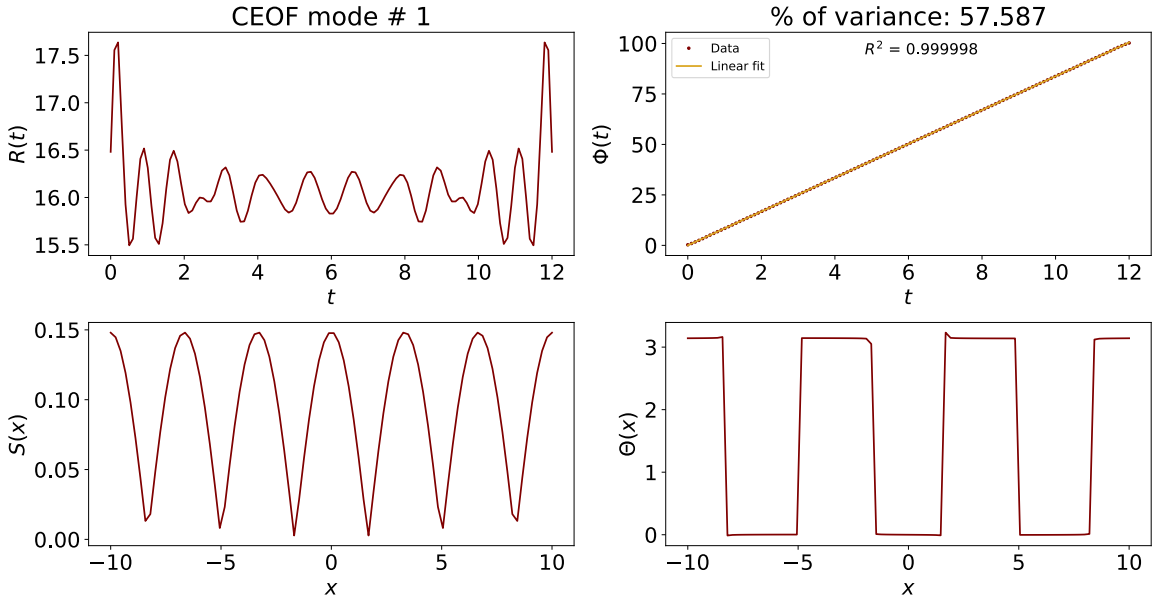

Figure 3.2: First CEOF mode of the one-dimensional test, corresponding to the standing wave. The four CEOF measures defined by Equations (2.9)–(2.12) are plotted.

Now we turn our attention to the temporal and spatial amplitudes, $R(t)$ and $S(x)$: see the left panels of Figure 3.1. We again compare Equations (3.1) and (3.5) and the last one leads us to expect that the product of these two quantities is constant and equal to A_p. We note that, except for the edge effects characteristic of Fourier analysis, $R(t)$ is practically constant indeed and the variations about its mean are smaller than 1%. On the other hand, $S(x)$ does not look constant at all, but we note that this function actually varies in a narrow range and presents oscillations around the average value which are smaller than 3%. To recover the amplitude A_p from the two measures $R(t)$ and $S(x)$ we multiply their average values, where the edges of $R(t)$ are first discarded. The result, which is presented in Table 3.1, is in excellent agreement with the actual amplitude of the propagating wave. The conclusion so far is that the CEOF analysis is well suited to obtain the features of one-dimensional propagating waves.

Next it is time to analyse the first CEOF mode, which accounts for 57.59% of the variance of the field. We note that Equations (3.1) and (3.3) look very different. The spatial phase function[1] of this CEOF mode (bottom right panel of Figure 3.2) gives us a clue of how these two formulas can be compared. We see that, except for some small irregularities that are analogous to Gibbs overshots and undershots, $\Theta(x) = \pi\ \mathrm{sq}(x)$. Here $\mathrm{sq}(x)$ denotes the unit square wave function, that is, a periodic function that is equal to 1 for half a period and to 0 for the other half period. Then, the factor $\exp[-i\Theta(x)]$ in Equation (3.1) reduces to either $+1$ or -1 when the spatial phase is 0 or π, respectively. Moreover, the spatial amplitude, $S(x)$, is maximum at $x = 0$ and oscillates like the absolute value of a cosine function, where the zeroes of $S(x)$ coincide with the transitions between 0 and π of $\Theta(x)$. Thus, except for a multiplying constant, the product $S(x)\exp[-i\Theta(x)]$ of Equation (3.1) reduces to the factor $\cos(k_s x)$ of Equation (3.3). The other factor in this formula is simply what remains in Equation (3.1), namely $\mathrm{Re}\{R(t)\exp[i\Phi(t)]\}$.

[1] To obtain the function $\Theta(x)$ of Figure 3.2 it has been necessary to add 2π to those values of this function that are below -0.1 rad. In this way, values of the spatial phase close to $-\pi$ have been converted to values near π.

The parameters of the standing wave can now be determined. First, following the procedure applied to the second CEOF mode, the frequency is obtained from a linear least-squares fit of $\Phi(t)$ vs t. It is worth mentioning that the square of the Pearson correlation coefficient is almost equal to one. Next, the wavelength is estimated from the distance between two consecutive transitions between 0 and π of $\Theta(x)$. And, finally, to compute the amplitude we see that $R(t)$ presents edge effects, as in the case of the propagating wave, although the oscillations around its mean do not exceed 3%. The product of the average of $R(t)$ and the maximum of $S(x)$ give us the estimation of A_s. Table 3.1 shows the obtained results, which are very close to the values used to generate the synthetic signal. So the CEOF method is also adequate to recover the features of one-dimensional standing waves.

A visual test of the CEOF modes can be achieved by means of the reconstruction given by Equation (2.15). Movies of the reconstruction can be found in this link. It is clear that the first two CEOF modes are the standing and propagating waves and their properties (A, ω and k) can be estimated from these movies. The third CEOF mode, on the other hand, displays an erratic behaviour that does not correspond to a wave. It seems to contain residuals of both W_p and W_s.

In general, the remaining variance in the other CEOF modes is not relevant and it corresponds to the imperfections of the method. Also, edge effects play a crucial role in the shape of the temporal amplitude function, but we have seen that its average is all we need to compute the wave amplitude. The study of this case has provided very useful and enlightening information about the four CEOF functions, although we must not forget, such as stated by Barnett (1983), that "however, [...] once the complexity of the field increases beyond several propagating features of irregular form, the easy interpretations are generally no longer possible, although some useful information can still be derived from the analysis".

3.2 Two-dimensional waves

3.2.1 Synthetic field

As in the one-dimensional study, the data input has been constructed by summing different propagating or standing waves. Adding another spatial dimension implies that the waves can propagate or be standing along two perpendicular directions. Using a Cartesian coordinate system, these are the x- and y-directions. We set $N_x = 90$, $N_y = 70$, $N_t = 120$, which means that the shape of the data cube is $90 \times 70 \times 120$ and that the spatial grid contains 6300 locations. Let us define the features of the two-dimensional test field, where the subscripts i, j, k and l in x_i, y_j, $\vec{r}_k$ and t_l are eliminated from this point.

The first component of this field is a wave that propagates along the direction given by the vector $\vec{k} = k_x\hat{x} + k_y\hat{y}$. Therefore, this is a two-dimensional propagating wave defined as

$$W_p(\vec{r}, t) \equiv W_p(x, y, t) = A_p \cos(\omega_p t - k_{xp}x - k_{yp}y), \tag{3.6}$$

where $\vec{r} = (x, y)$ and the values of A_p, k_{xp}, k_{yp} and ω_p are given in Table 3.2.

The second contribution to the field corresponds to a standing wave along the two directions

$$W_s(\vec{r}, t) \equiv W_s(x, y, t) = A_s \cos(k_{xs}x) \cos(k_{ys}y) \cos(\omega_s t). \tag{3.7}$$

Note that the spatial dependence has been separated as the product of two sinusoids. The values of A_s, k_{xs}, k_{ys} and ω_s can also be found in Table 3.2.

The third and last constituent has been baptised as a "mixed wave" and is a wave that is standing in the x-direction and propagates along the positive y-direction. It is given by

$$W_m(\vec{r}, t) \equiv W_m(x, y, t) = A_m \cos(k_{xm}x) \cos(\omega_m t - k_{ym}y). \tag{3.8}$$

This wave is built as the product of the two waves considered in the one-dimensional test case.

	Input data			CEOF results		
Wave type	Standing wave	Propagating wave	Mixed wave	Standing wave	Propagating wave	Mixed wave
A	2.378	1.457	3.465	2.419	1.455	3.490
k_x	1.571	1.885	1.257	1.553	1.881	1.271
k_y	0.898	2.244	0.942	0.897	2.243	0.943
ω	2.618	4.713	8.378	2.618	4.712	8.376
Mode variance				15.13%	21.98%	61.81%

Table 3.2: Test of the CEOF method with two-dimensional synthetic data. Arbitrary units are considered. The 2nd, 3rd and 4th columns give the wave parameters. The 5th, 6th and 7th columns provide the same parameters calculated from the CEOF analysis. The last row contains the percentage of the variance contribution of each CEOF mode.

So, the two-dimensional field is

$$V(\vec{r},t) = W_p(\vec{r},t) + W_s(\vec{r},t) + W_m(\vec{r},t). \tag{3.9}$$

As in the one-dimensional test, Table 3.2 holds the comparison between the synthetic parameters and the values obtained by the CEOF analysis. Again, the subscripts p, s and m denote whether the wave is propagating in both directions, standing in both directions or mixed.

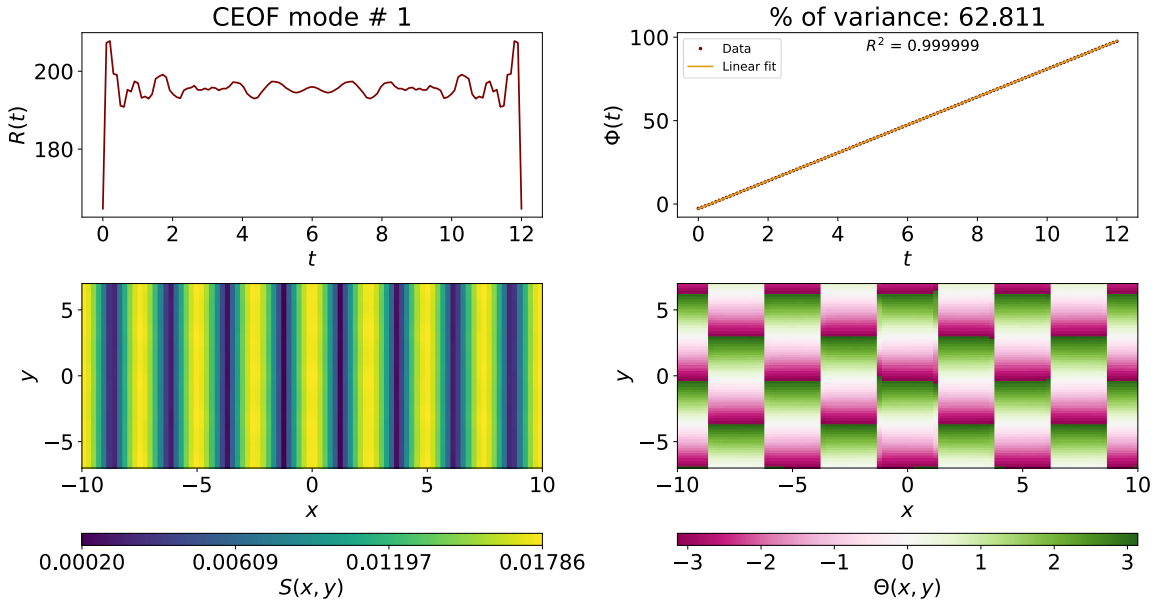

Figure 3.3: First CEOF mode of the two-dimensional test, corresponding to the mixed wave. The four CEOF measures defined by Equations (2.9)–(2.12) are plotted.

3.2.2 CEOF analysis

The CEOF method provides three dominant modes that hold 99.91% of the variance of the field. In order of decreasing variance, the first three CEOF modes contain 62.81%, 21.98% and 15.13% of the field variance and correspond to the mixed wave, the propagating wave and the standing wave, respectively. This distribution of variance of the total field was predictable since

the mixed wave has the greatest amplitude. We next explain how one can identify which wave corresponds to each CEOF mode.

First, the analysis of the temporal measures is analogous to the one-dimensional case. $\Phi(t)$ is a sawtooth function for each CEOF mode and so it is unwrapped again. As we can see in the top left panels of Figures 3.3–3.5, as a result of the unwrap the temporal phase presents a linear behaviour. A least squares linear fit to $\Phi(t)$ allows us to acquire the frequency of each mode; see Table 3.2. It is not surprising that the slope of the linear fit is equal to the wave frequencies of the synthetic signal with a high accuracy (note the values of the coefficient R^2, very close to unity). This allows us to identify which CEOF mode corresponds to each wave: CEOF modes #1, 2 and 3 can be associated with the mixed, propagating and standing waves. Of course, if we did not have information about the waves present in $V(\vec{r}, t)$, the other CEOF measures would enable us to reconstruct them, as we will see later. Next, the temporal amplitude, top right panels of Figures 3.3–3.5, has essentially the same behaviour for each of the first three CEOF modes. As in the one-dimensional case, $R(t)$ tends to a roughly constant value after stabilising for all modes. The oscillations around the average value do not exceed 4%. This is not surprising again since the wave amplitudes of the three waves do not depend on time. Let us now see what information is contained in the spatial measures.

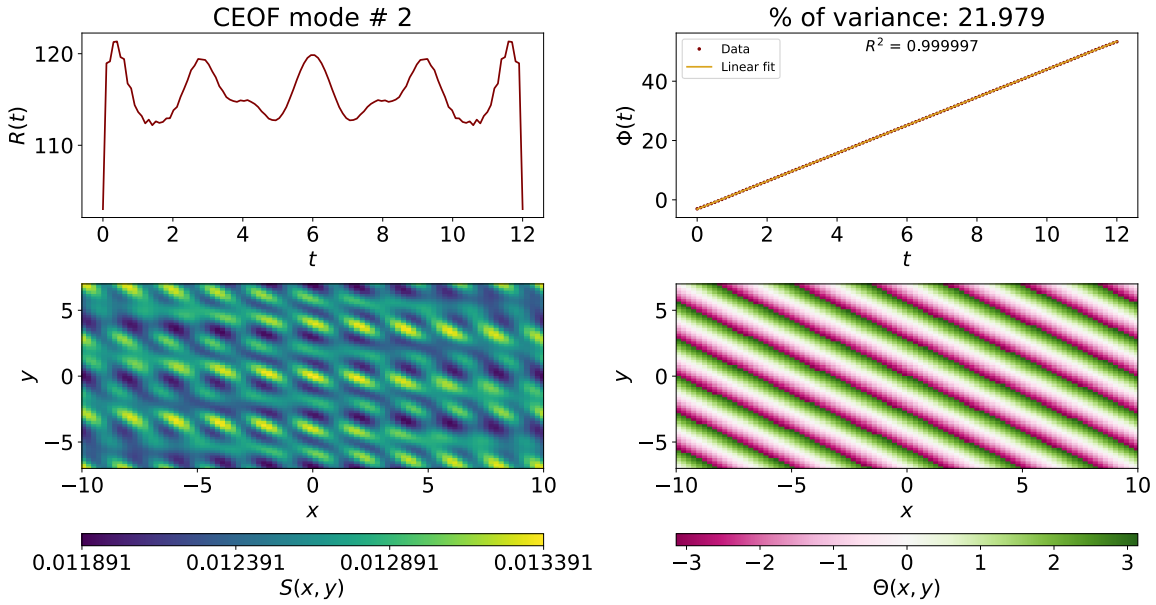

Figure 3.4: Second CEOF mode of the two-dimensional test, corresponding to the propagating wave. The four CEOF measures defined by Equations (2.9)–(2.12) are plotted.

We start our analysis of the spatial measures with the spatial amplitude of the first CEOF mode. The bottom left panel of Figure 3.3 shows that $S(\vec{r})$ does not vary appreciably in the y-direction and that there is a tiny but not negligible periodic oscillation along the x-direction. Because our constituent waves are separable in x and y it makes sense to do cuts of $S(\vec{r})$ for fixed x and y. These cuts for $y = N_y/2$ and $x = N_x/2$ are shown in the left panels of Figure 3.6. We can now appreciate that $S(\vec{r})$ has a weak dependence on y, with variations about the mean that do not exceed 1%, and that it has the shape of the absolute value of a cosine in the x-direction. These are the behaviours we already found in the one-dimensional test for a propagating and a standing wave, respectively: see the bottom left panels of Figures 3.2 and 3.1 for a comparison. As in the one-dimensional case, the amplitude of this wave can be obtained as the product of the average or $R(t)$ by the maximum value of $S(\vec{r})$. The obtained value, 3.490, is very close to the one used to construct $W_m(\vec{r}, t)$, namely 3.465 (for this and the other two CEOF modes, see Table 3.2 for the wave parameters inferred from the CEOF analysis). So this means that we

already have correctly inferred the frequency and amplitude of the mixed wave. This inference will be completed once the wavenumbers of these wave are obtained from $\Theta(\vec{r})$, but before doing so we also inspect $S(\vec{r})$ of the next two CEOF modes.

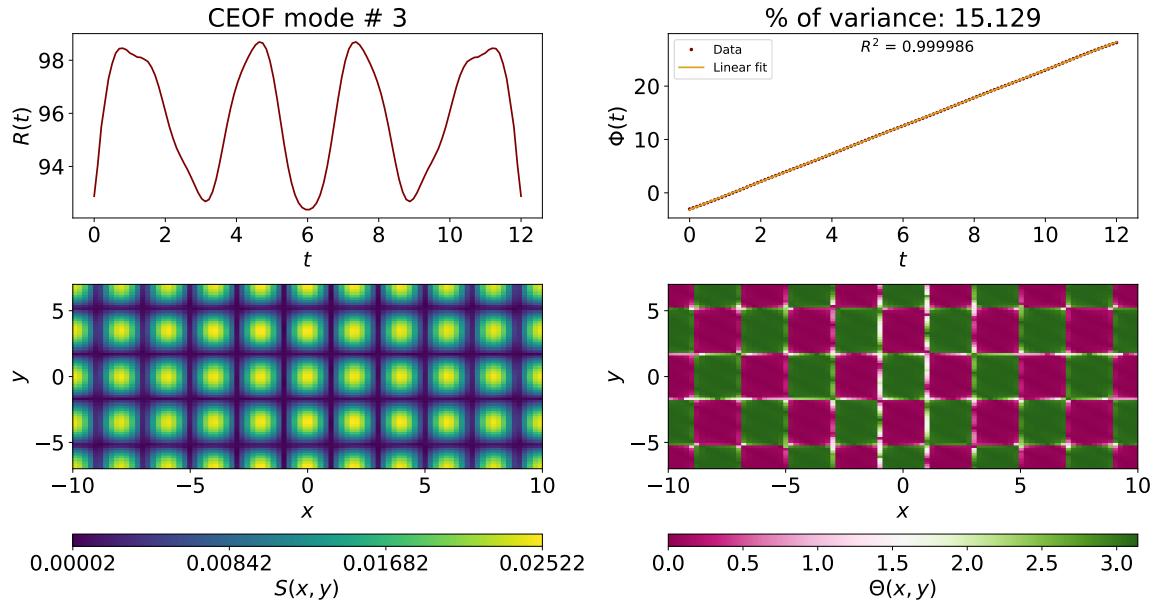

Figure 3.5: Third CEOF mode of the two-dimensional test, corresponding to the standing wave. The four CEOF measures defined by Equations (2.9)–(2.12) are plotted.

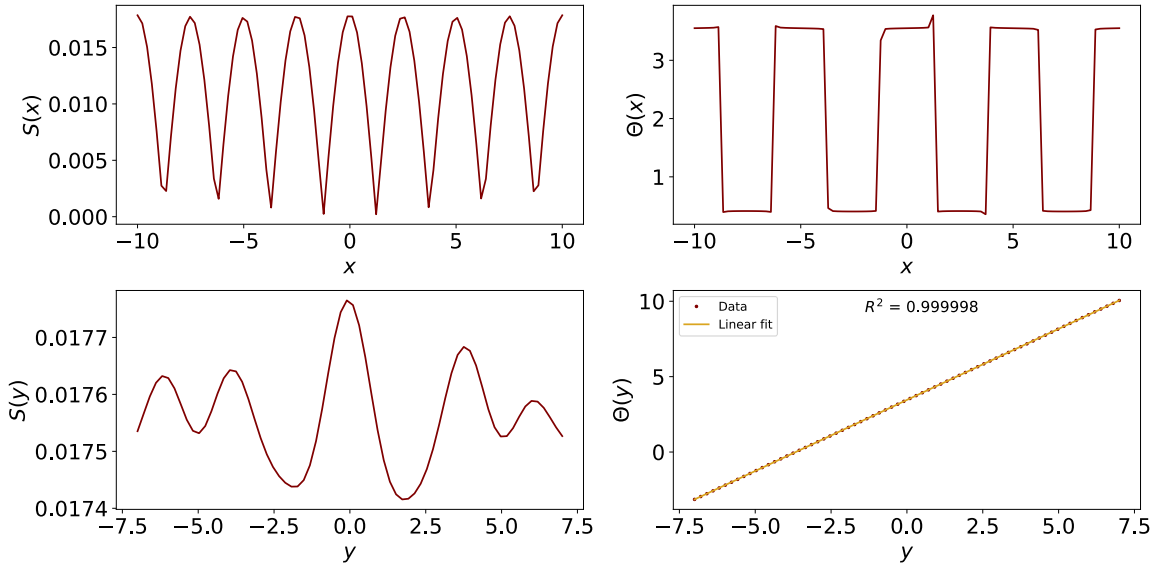

Figure 3.6: Cuts of the first CEOF mode of the two-dimensional test (Figure 3.3), corresponding to the mixed wave. The two CEOF spatial measures defined by Equations (2.9) and (2.10) are plotted for $y = N_y/2$ and $x = N_x/2$ in the top and bottom panels, respectively.

The spatial amplitude of the second CEOF mode is presented in Figure 3.4, bottom left panel. It displays some spatial structure, but we notice that the amplitude of its variations is rather small, less than 5%. Taking again two cuts along $y = N_y/2$ and $x = N_x/2$ (these cuts are not shown), it is immediate to observe that the behaviour seen in Figure 3.1 appears in both directions, so we can state that this CEOF mode is a propagating wave in the two directions. Its amplitude is calculated by multiplying the temporal average of $R(t)$ and the

spatial average of $S(\vec{r})$ and agrees quite well with the value used for $W_p(\vec{r},t)$. This evidence, together with its frequency, points to the second CEOF mode being the wave that propagates in the x- and y-directions. Finally, the spatial amplitude of the third CEOF mode (Figure 3.5, bottom right panel) looks like a chessboard, with well defined and regularly spaced nodes and maxima. Contrary to the previous two CEOF modes, these variations are not insignificant because the minima are close to zero. Moving along each of the two directions the oscillatory behaviour manifests itself with different length scales, which points to different wavenumbers in each direction. Cuts of $S(\vec{r})$ along $y = N_y/2$ and $x = N_x/2$ give a pattern like that of $S(x)$ of Figure 3.2, i.e. the absolute value of a cosine. Therefore, this CEOF mode corresponds to the standing wave, $W_s(\vec{r},t)$, whose amplitude is recovered as the product of the average of $R(t)$ times the maximum value of $S(\vec{r})$.

So far the analysis of the temporal measures and the spatial amplitude has provided the same conclusions about the identification of each CEOF mode with a particular wave. So it is time to analyse the spatial phase, which according to the one-dimensional test should be a combination of a linear or a square wave behaviour, or both, in the two spatial dimensions. It is worth to remember that the CEOF analysis returns Θ between $-\pi$ and $+\pi$ and that a linear behaviour is unveiled only after the phase is unwrapped. Without this operation, the spatial phase of a propagating wave does not show the linear behaviour of Figure 3.1, bottom right panel, but a sawtooth profile with vertical jumps between $\Theta = +\pi$ and $\Theta = -\pi$. It is essential to have this in mind to interpret some of the functions $\Theta(\vec{r})$ of Figures 3.3–3.5, bottom right panel. Once more let us start with the first CEOF mode (Figure 3.3). Its spatial phase presents two different behaviours. Along the y-direction $\Theta(\vec{r})$ gradually increases until it suddenly drops by an amount -2π. For different values of x, the behaviour is the same but the sawtooth shape is out of phase by half wavelength. In the y-direction, the spatial phase alternates between two values whose difference is π. Let us gain more insight with the help of cuts of $\Theta(\vec{r})$ along $y = N_y/2$ and $x = N_x/2$. They are presented in the right panels of Figure 3.6, where the phase unwrapping has been applied to the cut along $x = N_x/2$. The x- and y-dependence of Θ is analogous to those of Figures 3.2 and 3.1, respectively. Then, the first CEOF mode corresponds to a wave that propagates in the y-direction and is standing in the x-direction. As in the one-dimensional test case, the wavenumber k_y is given by the slope of the linear least-squares fit to $\Theta(y)$, while the wavenumber k_x is equal to 2π divided by the distance between two successive sudden upward or downward transitions. As evidenced by Table 3.2, both wavenumbers are in good agreement with those of $W_m(\vec{r},t)$ and this completes the retrieval of this wave's parameters from the CEOF analysis.

The spatial phase of the second CEOF mode (Figure 3.4) presents a visually simpler behaviour. We see that it remains constant along a particular direction that is inclined to the x- and y- axes. This direction is none other than the perpendicular to the wavenumber vector, $\vec{k}$, which indicates the propagation direction of $W_p(\vec{r},t)$. Moreover, in the direction of $\vec{k}$ we can detect the sawtooth behaviour characteristic of a propagating wave. Of course, this behaviour is also present in cuts along constant x and constant y, but the wavelength of the sawtooth is not the same. Once unwrapped, these cuts reproduce the linear variation of $\Theta(x)$ on Figure 3.1. Once more, a linear least-squares fit of the two cuts gives the two wavenumbers shown in Table 3.2 and the identification of the second CEOF mode with the propagating wave is complete.

Now, the spatial phase of the third CEOF mode has a chessboard arrangement. But contrary to the spatial amplitude, here the values inside the squares are constant and differ by π from those in the neighbouring squares. Thus, the spatial phase is the combination in the two directions of a square wave function, such as $\Theta(x)$ of Figure 3.2. This CEOF mode, as expected, corresponds to the standing wave and the computation of its wavenumbers can be done as explained above, leading to very accurate values. It should be mentioned that at the edges of the squares of $\Theta(\vec{r})$ there are pixels whose colour differs from the prevailing pink and green ones. This occurs

because abrupt changes in a function cannot be described well numerically. This also explains the irregularities at the edges of the plateaus in the spatial phase of Figure 3.6. Moreover, $\Theta(\vec{r})$ of Figure 3.5 seems to be contaminated from the spatial phase of the propagating wave. The CEOF analysis has not completely separated the two waves in two independent CEOF modes.

Once more, movies of the reconstruction of Equation (2.15) can be found in this link for the first four CEOF modes. The first three movies allow to visualise the temporal evolution of the mixed, propagating and standing waves, respectively. The fourth CEOF mode contains an initial transient and then becomes almost featureless in the scale of the movie. It does not contain a wave and the initial transient is probably caused by the edge effects we already found in $R(t)$.

The conclusion of this section is that the CEOF method is adequate to recover the features of the simple two-dimensional standing and propagating waves of our test field.

3.3 Two-dimensional waves with noise

When analysing real data it is very common to deal with signals that contain noise. This section will be useful to know how does the CEOF method work with this type of signals. It is also interesting to see which are the features of a CEOF mode whose origin is noise. So, to put the icing on the cake, the field given by Equation (3.9) is now modified by adding white noise uniformly distributed between -1.5 and $+1.5$, $N(t)$. In discrete time, white noise is a discrete signal whose samples are regarded as a sequence of serially uncorrelated random variables with zero mean and finite variance. So, the field becomes

$$V(\vec{r},t) = W_p(\vec{r},t) + W_s(\vec{r},t) + W_m(\vec{r},t) + N(t). \tag{3.10}$$

Nothing else is changed with respect to the latter section. The propagating, standing and mixed waves are defined by Equations (3.6), (3.7) and (3.8), respectively. The numerical parameters of the waves are shown again in Table 3.3. The same size of the data cube, i.e. $90 \times 70 \times 120$ has been considered. This way, all parameters are equal to those of the previous section and we can compare which changes have occurred owing to the addition of noise.

	Input data			CEOF results		
Wave type	Standing wave	Propagating wave	Mixed wave	Standing wave	Propagating wave	Mixed wave
A	2.378	1.457	3.465	2.419	1.455	3.490
k_x	1.571	1.885	1.257	1.510	1.884	1.266
k_y	0.898	2.244	0.942	0.886	2.237	0.942
ω	2.618	4.713	8.378	2.617	4.713	8.376
Mode variance				10.90%	15.61%	43.45%

Table 3.3: Test of the CEOF method with two-dimensional synthetic data and noise. Arbitrary units are considered. The 2^{nd}, 3^{rd} and 4^{th} columns give the wave parameters used in the equation (3.10). The 5^{th}, 6^{th} and 7^{th} provide the same parameters calculated from the CEOF analysis. The last row contains the percentage of the variance contribution of each CEOF mode.

The main difference from the previous case is that now the three CEOF modes associated to actual waves only hold $\sim 70\%$ of the variance of the field of Equation (3.10); see last line of Table 3.3. This is not surprising since the maximum value of $N(t)$ is 1.5, slightly greater than A_p and smaller than but still of the order of A_s and A_m. The mixed wave has lost almost 20%

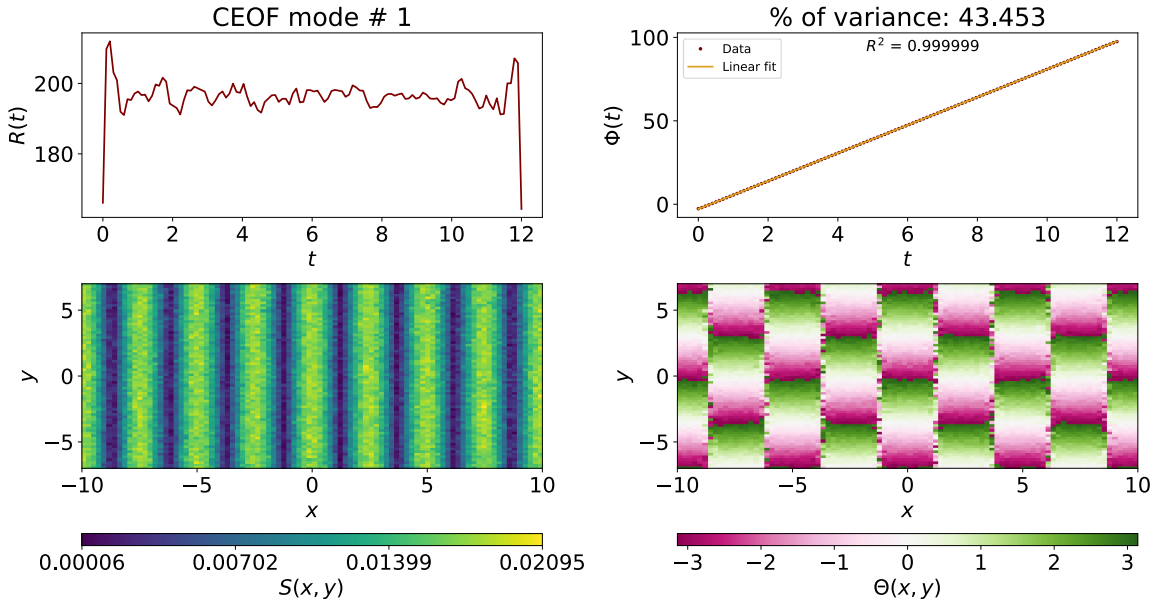

Figure 3.7: First CEOF mode of the two-dimensional test with noise, corresponding to the mixed wave. The four CEOF measures defined by Equations (2.9)–(2.12) are plotted.

of its previous contribution to the variance. The other two CEOF modes have only diminished their contribution to the field variance by 5%.

Due to lack of space, only the measures and the cuts of the first CEOF mode are shown; see Figures 3.7 and 3.8. We will compare them with Figures 3.3 and 3.6, respectively. The first impression is that all figures look blurred in the present case, except for $\Phi(t)$. The temporal amplitude presents similar values in the two cases, but it is more wiggly when noise is included in the synthetic signal. In addition, the temporal phase looks unchanged, the coefficient R^2 is the same, at least up to the first six decimal places, and the frequency, equal to the slope of the linear least-squares fit remains excellent when compared with the value used in $W_m(\vec{r}, t)$; see Table 3.3.

The spatial part of the first CEOF mode shows the biggest differences between the noiseless and noisy cases. A quantitative comparison can be performed with the cuts of Figures 3.6 and 3.8. In Figure 3.8 the shape of $S(x)$ is still reminiscent of the absolute value of a cosine function, but it is not as neat as in Figure 3.6. Also $S(y)$ has small variations about the mean value, but they are larger in the signal with noise. The square wave shape of $\Theta(x)$ is also strongly modified now, especially at the $\pm\pi$ phase jumps, but still an accurate estimation of the wavelength can be attained. And, finally, the linear behaviour of $\Theta(y)$ remains, although with a poorer, but quite good, correlation coefficient. The spatial wave parameters have been obtained in the same way as in the previous section. They are presented in Table 3.3. Comparing Tables 3.2 and 3.3 we note that they are modified only in a few decimal numbers, but the differences are not too important. Therefore, adding noise to our test signal does not compromise the CEOF performance.

The analysis of the next two CEOF modes follows the steps described in the previous section. We find the same features of CEOF mode #1, namely noisier temporal and spatial functions, although reliable information on the wave type and specific values of its frequency and wavenumber can be derived. See Table 3.3 for a summary of results.

The remaining variance in the other CEOF modes corresponds, on the one hand, to the imperfections of the method and, on the other hand, to the noise. The CEOF method has separated this latter ingredient in thirty modes that contribute between 0.5 and 0.6% to the total variance of the field. They posses essentially random $R(t)$, $S(\vec{r})$ and $\Theta(\vec{r})$. The function

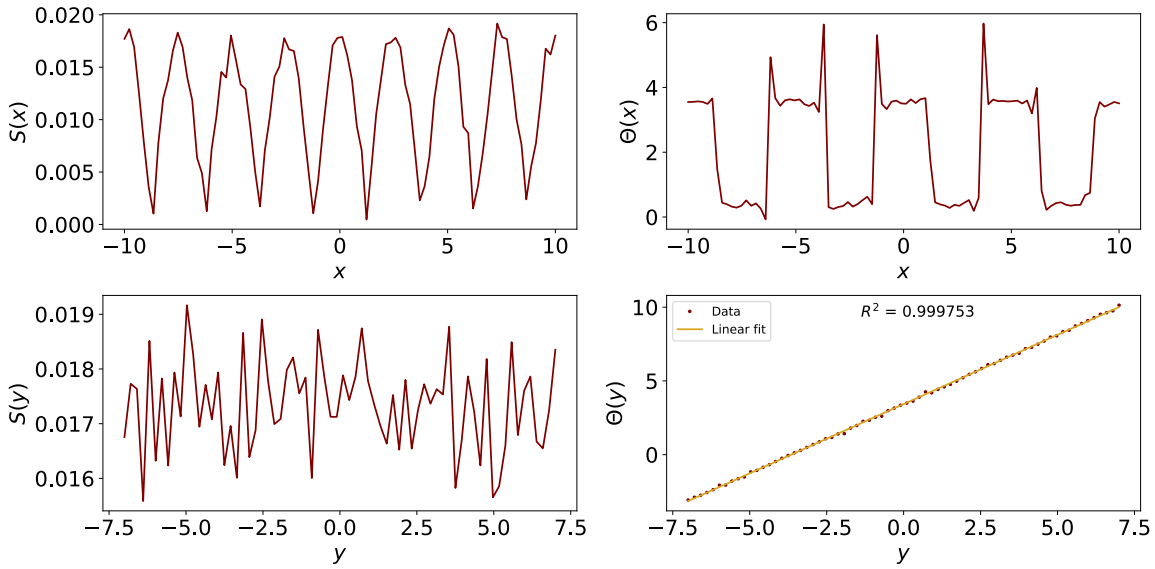

Figure 3.8: Cuts of the first CEOF mode of the two-dimensional test with noise (Figure 3.7), corresponding to the mixed wave. The two CEOF spatial measures defined by Equations (2.9) and (2.10) are plotted for $y = N_y/2$ and $x = N_x/2$ on top and bottom panels, respectively.

$\Phi(t)$ may look linear, but the randomness of the other three measures is an indication that the CEOF mode is irrelevant and has no physical meaning.

The reconstruction of Equation (2.15) for the first three CEOF modes now gives noisier animations than in the case without noise; these animations can be found in this link. This is the expected result. The fourth CEOF mode is much more dominated by noise than the same mode of Section 3.2.

Our tests finish here. We can conclude that the CEOF method has passed the examination outstandingly because it has provided the amplitude, frequency and wavenumber of the three waves with good accuracy, despite the addition of noise. However, in the real world well defined, noiseless fields are exceptional. So let us now see how the CEOF method works with non-linear waves.

Chapter 4

Oscillations in the solar tachocline

4.1 Introduction

The Sun's tachocline is an extremely thin region, with a thickness $\sim 0.03 R_\odot \sim 21$ Mm, that is sandwiched between the inner radiative zone and the outer convective zone. Thus, the tachocline marks a steep transition from the radiative interior, that rotates like a rigid body, and the outer convective envelope, that displays differential rotation both in the radial and in the latitudinal directions. For reasons that are beyond the scope of this work and that are linked to this strong velocity shear, the solar tachocline seems to play a major role in the storage and amplification of solar magnetic fields (see Section 6.3 of Charbonneau 2020). These magnetic fields are stored in buoyant flux tubes that emerge toward the solar surface and form sunspots, which are a manifestation of solar activity.

It has been recently appreciated that the study of the tachocline dynamics is valuable to understand solar activity in different time scales, from months to years. For example, Dikpati et al. (2017) suggested that the interaction between differential rotation and Rossby waves can produce bulges at the top of the tachocline, which facilitate the emergence of magnetic flux stored there. Dikpati et al. (2017) used the hydrodynamic shallow-water approximation to describe the non-linear physics of the tachocline. This model and its assumptions are described in Dikpati & Gilman (2001) and Dikpati (2012), who states that, owing to the small tachocline thickness, "the divergence of radius and the density variation within the shallow fluid layer are ignored in the momentum and mass-continuity equations. All timescales of the system are considered much longer than the acoustic timescale." Hence, there is no radial dependence of the variables in a shallow-water model, which are functions of time, t, longitude, ϕ, and latitude, θ[1]. The hydrodynamics of the tachocline are described in terms of three dependent variables: the tachocline thickness, h, and the longitudinal and latitudinal velocity components, u and v. These variables are governed by three non-linear, time dependent partial differential equations that are not reproduced here. They are Equations (4)–(6) of Dikpati (2012) and are given in dimensionless units, where one time unit is $\sim 3.2 \times 10^5$ s and one length unit is $\sim 4.9 \times 10^8$ m. Consequently, the speed unit is $\sim 1.5 \times 10^3$ m s^{-1}. The governing equations of h, u and v are solved in a rotating frame of reference, meaning that perturbations travelling to the right (left) are prograde (retrograde). The tachocline is not a rigid body but displays differential rotation, that is, a latitudinal variation of the rotation rate. Thus, from the point of view of the rotating reference frame, the presence of differential rotation implies that u is not zero at all latitudes, but only at those that rotate with the same angular velocity of the reference frame. This issue is discussed in more detail in Section 4.3.1.

It is of relevance to this work the process of energy interchange between differential rotation and Rossby waves found by Dikpati (2012) and Dikpati et al. (2017). In the numerical simulation

[1]Note that the angular coordinates in a spherical coordinate system, ϕ and θ, are written in small letters, while the CEOF temporal and spatial phases, Φ and Θ, are written in capital letters

analysed here differential rotation is unstable and then Rossby waves can grow by draining kinetic energy from the flow. These waves then increase their amplitude and enter a non-linear regime in which differential rotation is modified in such a way that it can no longer provide more energy to Rossby waves. Next, waves feed back energy to the flow and their amplitude declines, the latitudinal profile of differential rotation is restored to its previous shape and the whole process can repeat again. In this phenomenon the tachocline thickness also oscillates, reaching its maximum value at the stage when Rossby waves have gained the maximum possible energy from differential rotation.

In this chapter the CEOF method will be applied to the two-dimensional fields $h(\phi, \theta, t)$, $u(\phi, \theta, t)$ and $v(\phi, \theta, t)$ of a numerical simulation used in Dikpati et al. (2017). Each of these three variables is discretised on a mesh of $N_\phi = 80$ by $N_\theta = 195$ by $N_t = 11\,741$ points, with $0 \leq \phi \leq 2\pi$ rad, $-\frac{\pi}{2}$ rad $\leq \theta \leq \frac{\pi}{2}$ rad and $0.08256 \leq t \leq 458.9378$. Animations of each variable can be downloaded in this link. All three variables display a pattern that travels from right to left, which points to the presence of travelling retrograde waves. This pattern has a time-dependent amplitude. For example, the blue- and red-coloured bands of u change the intensity with time in an apparently periodic manner. The same happens to the blue colours of h. Periodic variations can also be observed in v near the equator, although they are more difficult to detect. The travelling disturbances of h and u are superposed to bands parallel to the equator. All these features will be recovered as individual CEOF modes.

The time values are not equally spaced and have an average $\Delta t = 0.03908$. In addition, solving the CEOF problem for a $80 \times 195 \times 11\,741$ data cube is intractable and a reduction in the number of temporal values is necessary. We decided to retain only $N_t = 100$ points and selected them so as to minimise the variations of $t_{l+1} - t_l$. The chosen times have an average $\Delta t = 4.635$, with minima and maxima equal to 4.598 and 4.665, respectively. The CEOF analysis requires Δt to be constant, but we will apply it and will ignore this small dispersion of Δt values.

From now on the subscripts i, j and k in the spatial coordinates and l in time are removed unless they become necessary.

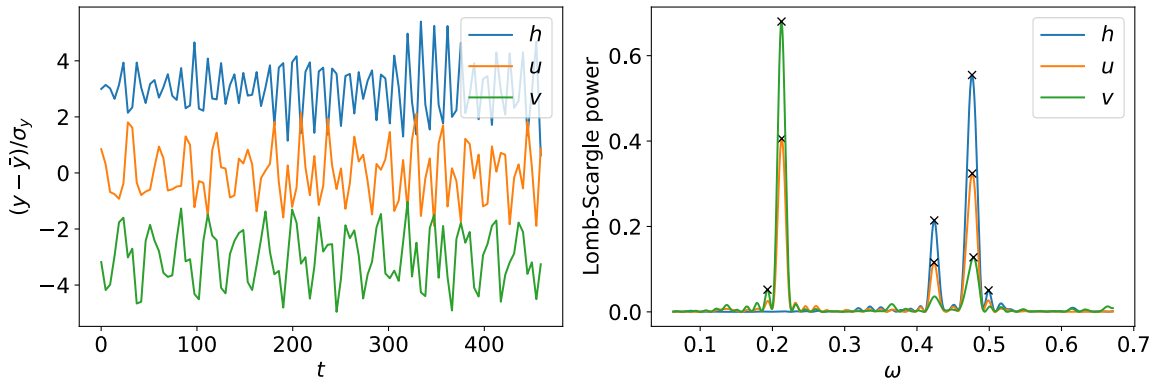

Figure 4.1: Left panel: h, u and v as a function of t at the position $\phi_i = 4.5°$, $\theta_i = 7.423°$. Before plotting the functions each of them has been transformed as follows: first, the function minus its mean has been divided by the signal standard deviation. Second, a vertical shift of $+3$ and -3 has been applied to h and v, respectively. Right panel: Lomb-Scargle periodograms of the signals of the left panel. The standard normalisation, for which the periodogram is dimensionless and lies between 0 and 1, has been used (VanderPlas 2018). Crosses mark the maxima whose power is above 0.1.

4.2 Frequencies and wavenumbers

Before executing our CEOF code, we explore the presence of periodic signals in the three variables. For this purpose we use the Python implementation of the Lomb-Scargle periodogram (https://docs.astropy.org/en/stable/timeseries/lombscargle.html); see VanderPlas (2018). We select a pair of points with coordinates ϕ_i and θ_j and compute the power spectra of $h(\phi_i, \theta_j, t)$, $u(\phi_i, \theta_j, t)$ and $v(\phi_i, \theta_j, t)$. The example of Figure 4.1, left panel shows that the three variables contain oscillations with different periods. The Lomb-Scargle periodogram of these signals (Figure 4.1, right panel) gives the values of these periods: the frequency $\omega = 0.213$ is present in both u and v, while $\omega = 0.424$ and $\omega \sim 0.4767$ appear in the three signals. At this point we note that the second frequency is twice the first one.

Next, the Lomb-Scargle periodogram is calculated for all positions (ϕ_i, θ_j) and the frequencies of power peaks are retained. This allows us to have an idea of the periodicities present in h, u and v over the whole tachocline surface. We select peaks whose power is above 0.1. This value cannot be too small or else spurious peaks caused by discrete sampling and leakage will not be rejected. Examples of spurious peaks are probably the two with black crosses with $\omega \sim 0.2$ and $\omega \sim 0.5$ in Figure 4.1, right panel. On the other hand, discarding peaks below the 0.1 power level may lead to the rejection of true periodic signals, such as that of v at $\omega = 0.424$. So we must be ready to accept that the histogram of frequencies, displayed in Figure 4.2, is incomplete. Apart from the three frequencies detected in Figure 4.1, we can also appreciate a band of periodicities of h around $\omega = 0.07 - 0.09$. The total number of pairs (ϕ_i, θ_j) is 15 600, hence the periodicities at $\omega \sim 0.21$, $\omega \sim 0.42$ and $\omega \sim 0.48$ are widespread in the spatial domain.

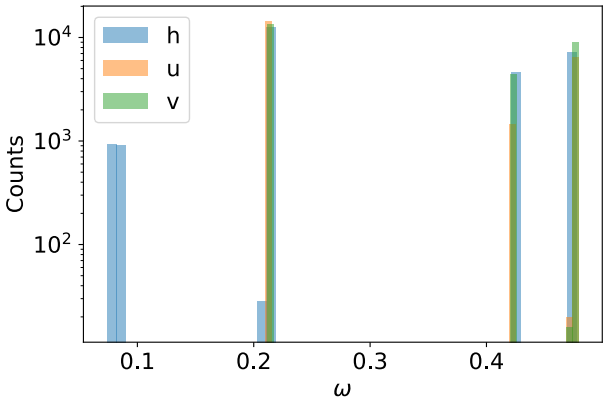

Figure 4.2: Histogram of frequencies of peaks in the Lomb-Scargle periodogram whose power is greater than 0.1, where all positions (ϕ_i, θ_j) have been used.

4.3 CEOF results

We have applied the CEOF method to each of the variables h, v and u separately with the purpose of finding physical modes of oscillation in the numerical simulation. We set $N_\phi = 80$, $N_\theta = 195$, $N_t = 100$, so the shape of the data cube is $80 \times 195 \times 100$ for each variable. The spatial mesh contains 15 600 locations. Keeping in mind that we are using spherical coordinates, the position vector is $\vec{r} = (\phi, \theta)$.

4.3.1 Tachocline differential rotation

The first CEOF mode of both h and u can be associated to the tachocline differential rotation. These modes contain 99.974% and 83.463% of the variance of their respective fields. As we can see in Figure 4.3, the temporal amplitude of h remains almost constant. Note that for $t \geq 200$,

however, $R(t)$ fades slightly. The temporal amplitude of u looks quite similar to that of h, but the amplitude of the oscillations is larger now. It is possible that the temporal amplitude variations are due to energy exchange between differential rotation and Rossby waves present in the field, as explained above.

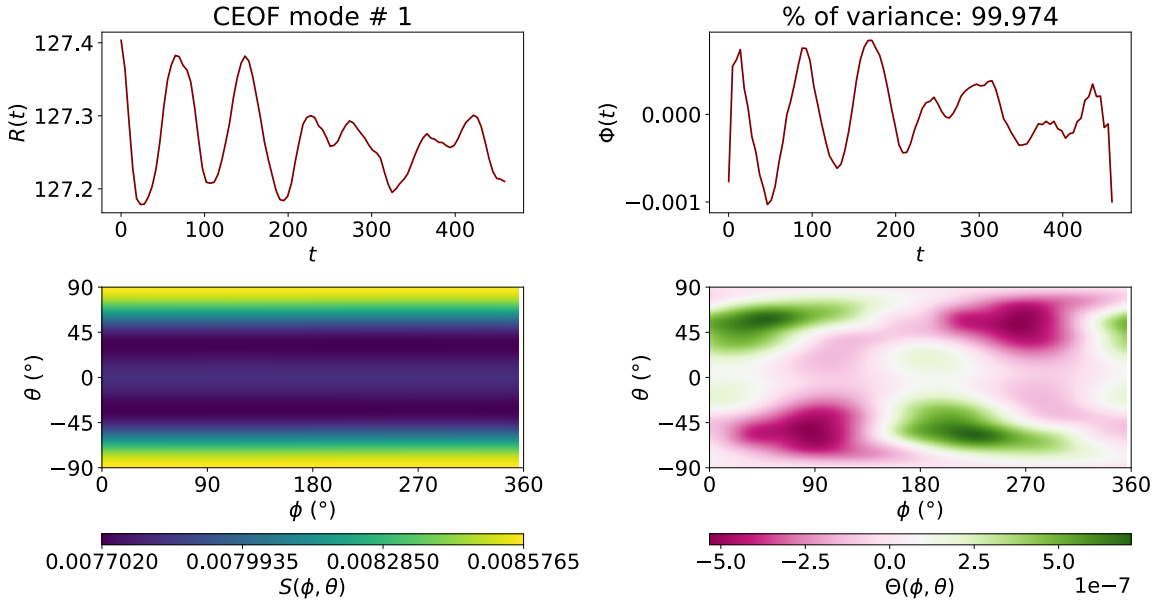

Figure 4.3: First CEOF mode of h, corresponding to the tachocline rotation. The four measures defined by Equations (2.9)–(2.12) are plotted.

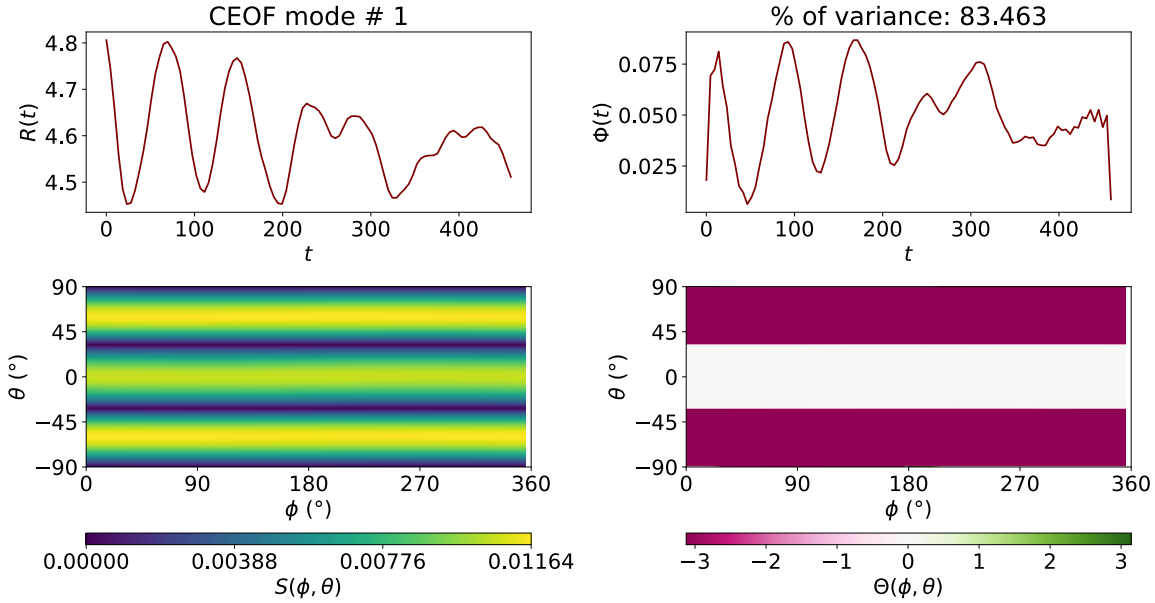

Figure 4.4: First CEOF mode of u, corresponding to the tachocline rotation. The four measures defined by Equations (2.9)–(2.12) are plotted.

The clue that confirms that this CEOF mode is not a wave lies in the temporal phase of h and u. It does not present a linear dependence with ϕ. Instead, it is practically zero. In addition, the spatial phase is negligible for h and is either 0 or $-\pi$ for u. Hence, the exponential term in Equation (2.15) is practically equal to 1 for h and is either approximately equal to 1 or -1 for u. The final bit of information comes from the spatial amplitude distribution. In the case of h,

$S(\phi, \theta)$ is everywhere positive and larger at poles than at the equator. Thus, differential rotation makes the tachocline thinner at the equator and thicker the poles. Regarding u, recall that the spatial phase leads to a factor -1 at high latitudes. Therefore, the two yellow stripes of $S(\phi, \theta)$ at latitudes above 45° imply a negative sign. This means that this velocity component is directed to the right (left) in a band around the equator (near the poles). To interpret this result we must remember that the numerical solution is obtained in an inertial reference frame rotating with a specific angular velocity, equal to that of the tachocline at $|\theta| \sim 35°$. In addition, the differential rotation is faster at the equator and slower at the poles. Then, in the inertial reference frame the longitudinal velocity component is zero at $|\theta| \sim 35°$, positive below this latitude and negative at higher latitudes. And this is precisely what we find in the plot of $S(\phi, \theta)$: the positive and negative values are separated by two dark horizontal bands at $|\theta| \sim 35°$. Finally, the distribution of the spatial phase has a strong azimuthal symmetry for both h and u, such as expected for the differential rotation.

Note that these rotation effects have not been found in the latitudinal velocity component, v. This is not surprising since the tachocline rotation is perpendicular to the ϕ-direction and v is the velocity component in the θ-direction.

Wave	$\omega \sim 0.21$			$\omega \sim 0.47$			$\omega \sim 0.22$
CEOF mode	h mode #2	u mode #2	v mode #1	h mode #3	u mode #3	v mode #2	v mode #3
A	0.024	0.011 / 0.007	0.020/ 0.006	0.009 / 0.004	0.003 / 0.001	0.009	0.002
$k_\phi(\text{rad}^{-1})$	-0.998	-0.999	-0.996	-1.998	-1.999	-1.988	-1.144
$k_\theta(\text{rad}^{-1})$	2.00	2.50	2.00	1.00	3.00	2.00	3.66
ω(rad)	0.213	0.213	0.213	0.470	0.468	0.470	0.221
Mode variance	0.022%	13.773%	78.436%	0.003%	2.114%	19.126%	0.565%

Table 4.1: CEOF method applied to the hydrodynamic numerical simulation of the tachocline. Columns provide the wave parameters calculated from the CEOF analysis for each of the CEOF modes of each variable. The last row contains the percentage of the variance contribution of each CEOF mode to its field. Whenever the amplitude changes in space or time, its minimum and maximum values are given in the corresponding cell. As explained in the text, the values of k_θ are approximate.

4.3.2 Wave with frequency near 0.21

In this section we present evidence that the second CEOF mode of h and u and the first CEOF mode of v have wave properties. Their CEOF measures are shown in Figures 4.5–4.7. First of all, their temporal phase has an almost perfect linear dependence (see the values of the R^2 coefficient in the top right panels of these figures). The frequency of these CEOF modes, equal to the slope of their temporal phase, is $\omega \sim 0.21$ and this means that one wave is responsible for the generation of all of them. For this reason, they are now analysed together. Their amplitude, wavenumbers and frequency and contribution to the field variance are presented in Table 4.1. We can see that the CEOF mode of h contributes very little to the total variance, a tiny 0.022%, and still it is significant from the physical point of view and its wave features can be retrieved well from its four CEOF measures. The CEOF modes of u and v both contribute with larger amount to their respective total variance, namely 14% and 78%.

We follow our analysis of this wave with the temporal amplitude. We see that it displays the same shape for the three variables, namely oscillations with a similar period and variations between 15 and 20% about their mean. Moreover, $R(t)$ possesses a clear decreasing trend. Such

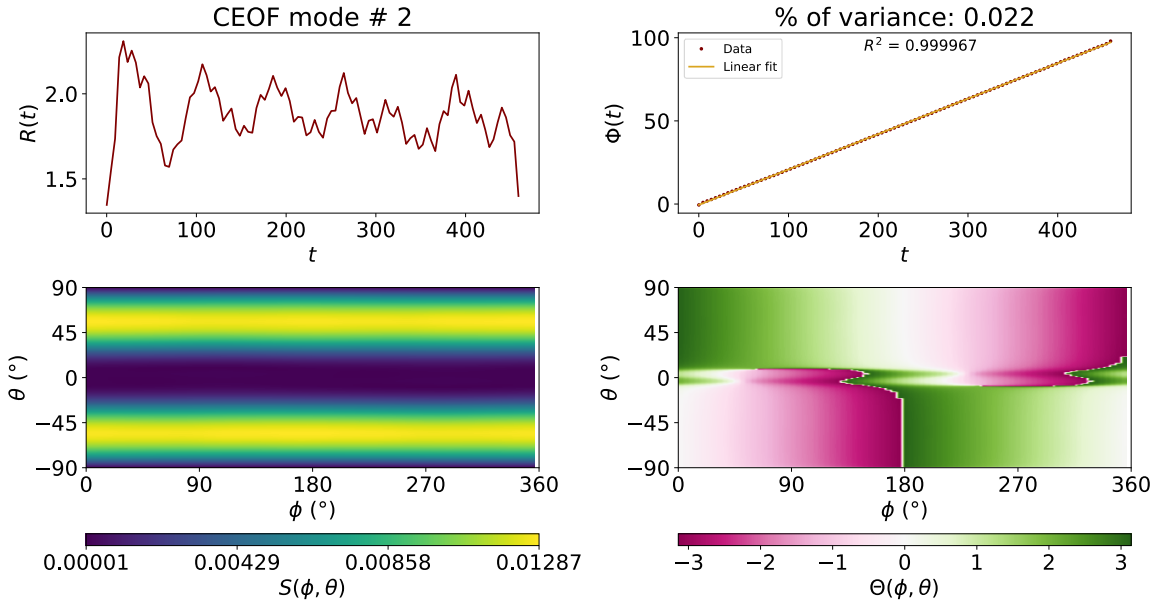

Figure 4.5: Second CEOF mode of h, corresponding to the wave with $\omega \sim 0.21$. The four measures defined by Equations (2.9)–(2.12) are plotted.

large changes of $R(t)$ can be a sign of the interchange of kinetic and potential energy found by Dikpati (2012) and Dikpati et al. (2017).

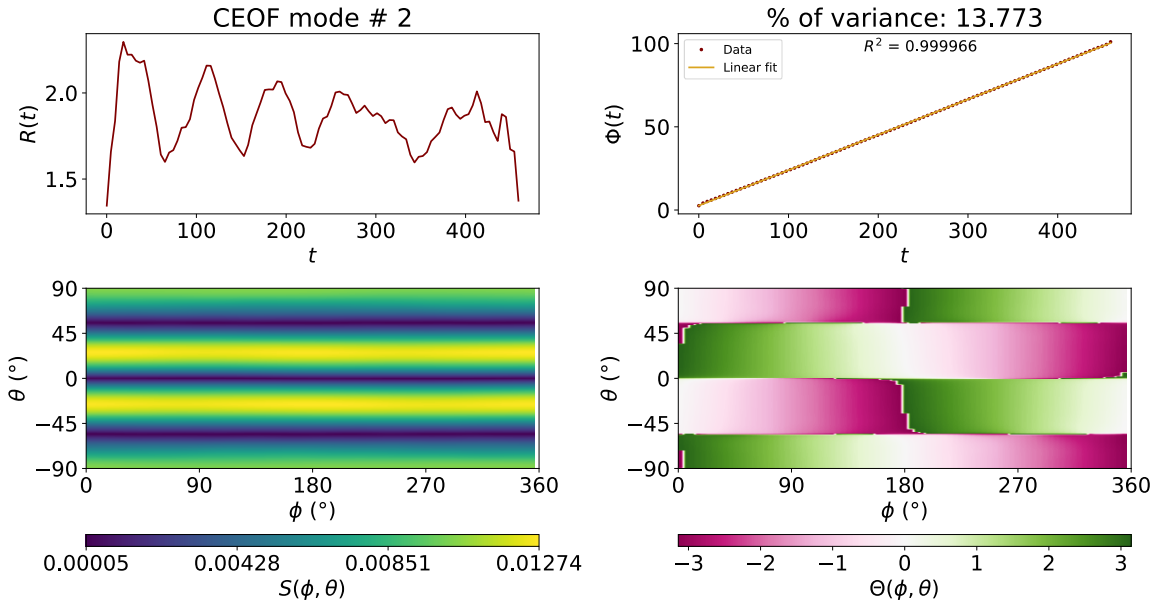

Figure 4.6: Second CEOF mode of u, corresponding to the wave with $\omega \sim 0.21$. The four measures defined by Equations (2.9)–(2.12) are plotted.

The next measures to be inspected are the spatial amplitude and phase. The analysis is simplified if we compare $S(\phi, \theta)$ and $\Theta(\phi, \theta)$ from Figures 4.5–4.7 with $S(x, y)$ and $\Theta(x, y)$ of Figure 3.3. Their properties are identical, with ϕ and y playing the role of the direction of wave propagation and x and θ playing the role of the direction along which the wave is standing. Hence, the wave responsible for the three CEOF modes under scrutiny propagates in the ϕ-direction and is standing in the θ-direction. In the terminology of our two-dimensional tests, it is a mixed wave. We now continue with the spatial phase. The cuts of $S(\phi, \theta)$ and $\Theta(\phi, \theta)$ in the

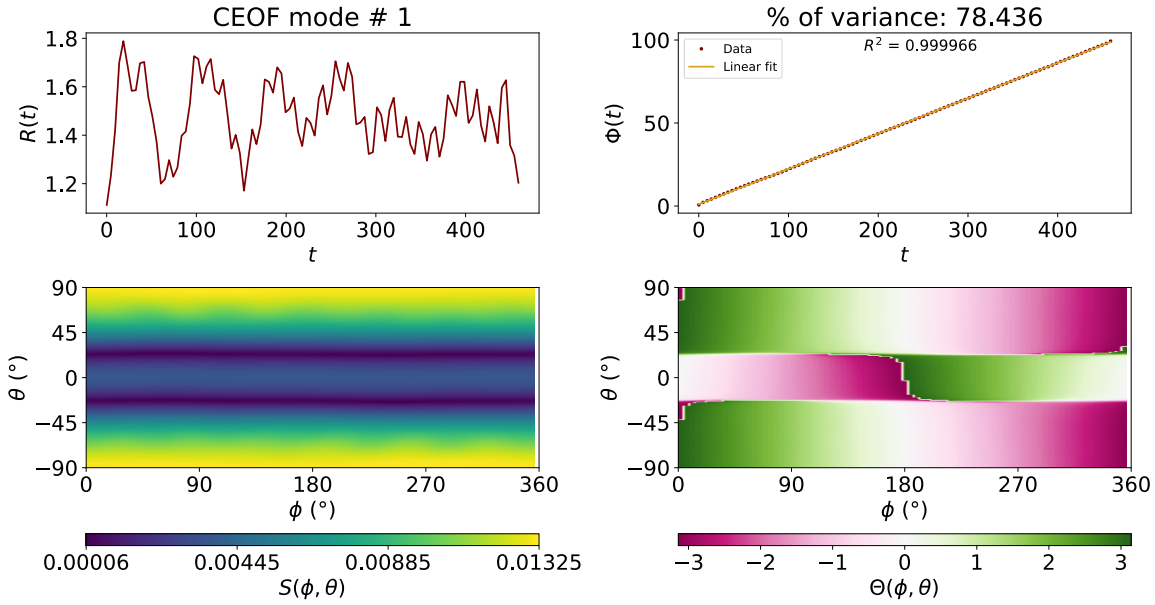

Figure 4.7: First CEOF mode of v, corresponding to the wave with $\omega \sim 0.21$. The four measures defined by Equations (2.9)–(2.12) are plotted.

latitudinal and longitudinal directions presented in Figures 4.8 and 4.9 will help our discussion. These cuts are for the CEOF modes of h and v. A linear least-squares fit to $\Theta(\phi)$ shows that the wave has $k_\phi \sim -1$ rad^{-1}, which means that the wavelength in this direction is $\lambda_\phi \sim 2\pi$. Because of the periodicity of waves on a sphere in the ϕ-direction, an integer number of wavelengths must fit in the interval $0 \leq \phi \leq 2\pi$. Hence, this mode has the longest possible wavelength, i.e. it is the fundamental mode in the longitudinal direction. The negative sign of k_ϕ point to this wave propagating against the direction of rotation, such as corresponds to a Rossby wave. The wavenumber k_θ has a surprise: first, it differs between the three variables, and, second, it is not constant for the CEOF mode of v. In this particular case, see Figure 4.7 and the bottom right panel of Figure 4.9, we see that the equatorial band is narrower than the other two at higher latitudes. An estimation of k_θ has been obtained as in Sections 3.2 and 3.3, i.e. by computing the wavelength from the distance between different sudden vertical transitions of $\Theta(\phi, \theta)$. In the modes analysed in this chapter, this distance can correspond to half a wavelength, a full wavelength (such as happens with Figure 4.8, bottom right panel) or one and a half wavelengths.

All that remains is the spatial amplitude, which presents almost perfect azimuthal symmetry. Also, it is minimum at the equator for h and u, but attains a small maximum for v. The maxima of h around 60° coincide with two minima of u, which has four maxima: two at lower latitudes and two more at the poles. The latitudes at which v is maximum or minimum are not relevant locations of the other two variables. The maxima of v are located at the poles.

Let us get a deeper insight into the spatial structure of the eigenfunctions from the cuts of Figures 4.8 and 4.9. They both allow us to appreciate the slight, almost negligible dependence of the spatial amplitudes with the ϕ-coordinate and their non-sinusoidal profile in the θ-direction. In particular, the spatial amplitude of the first CEOF mode of v has a θ-dependence that is analogous to that of a stationary wave with non-constant amplitude. Note that, because of the structure of $\Theta(\phi, \theta)$, the lateral lobes a positive sign, wheres the central lobe has a negative sign. The presence of two amplitudes in this CEOF mode leads us to show both of them in Table 4.1. Finally, the non-constant k_ϕ in Figure 4.9 can be clearly appreciated.

The parameters ω, k_ϕ and k_θ of the three CEOF modes studied in this section can be found in Table 4.1. The amplitude is also shown in this table. It has been calculated as in Sections 3.2 and 3.3 for the mixed wave: the temporal average of $R(t)$ is multiplied by the maximum of

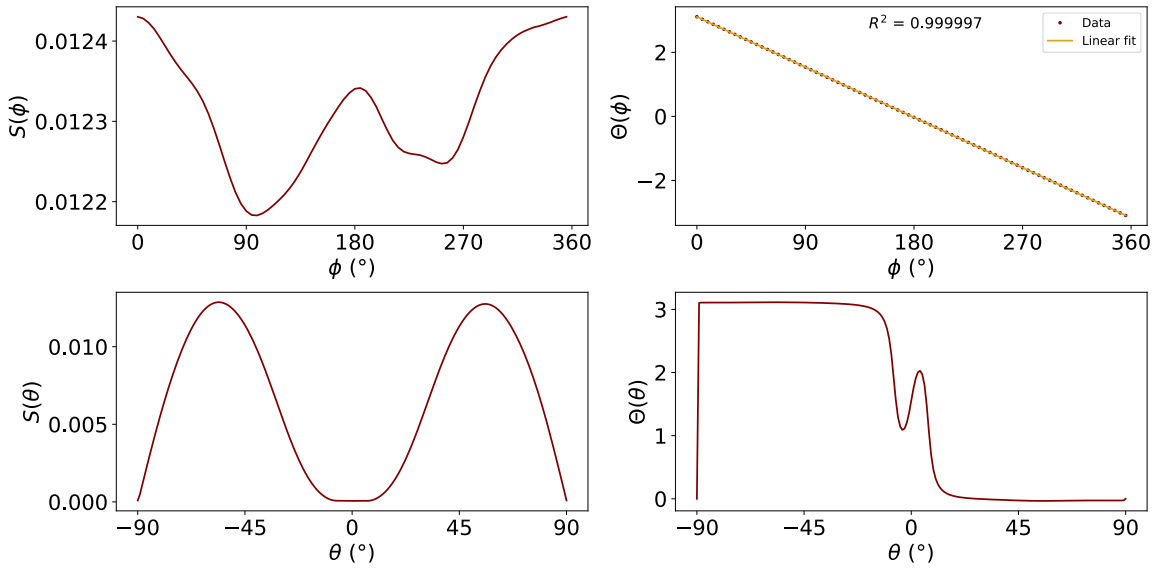

Figure 4.8: Cuts of the second CEOF mode of h, shown in Figure 4.5. The two CEOF spatial measures are plotted for $\theta \sim 50°$ and $\phi \sim 90°$ in the top and bottom panels, respectively.

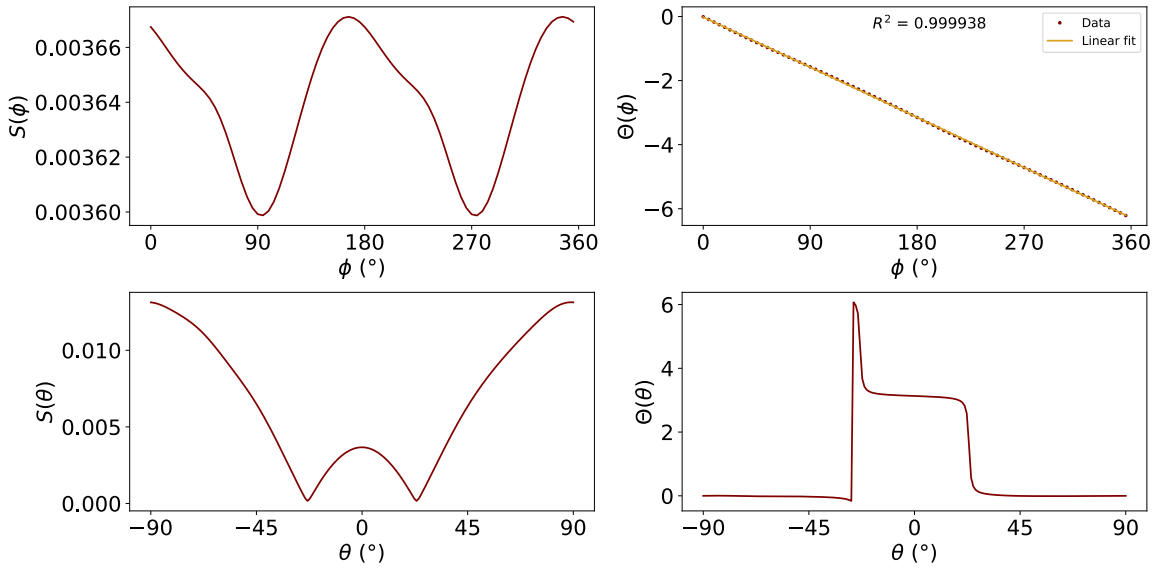

Figure 4.9: Cuts of the first CEOF mode of v, shown in Figure 4.7. The two CEOF spatial measures defined by Equations (2.9) and (2.10) are plotted for $\theta = 7N_\theta/9$ and $\phi = N_\phi/2$ in the top and bottom panels, respectively.

$S(\phi, \theta)$. The comparison of the wave properties determined in our analysis with those of Rossby waves in the present tachocline model are left for future work.

Animations of the three CEOF modes associated to the present wave are provided in this link. Retrograde propagation with a roughly constant amplitude can be observed in the three variables, with a different spatial structure in each of them.

4.3.3 Wave with frequency near 0.47

The next three CEOF modes of h, u and v in descending order of variance also share a common frequency. Again, the obvious explanation is that these disturbances are caused by the same wave. Its properties are presented in Table 4.1.

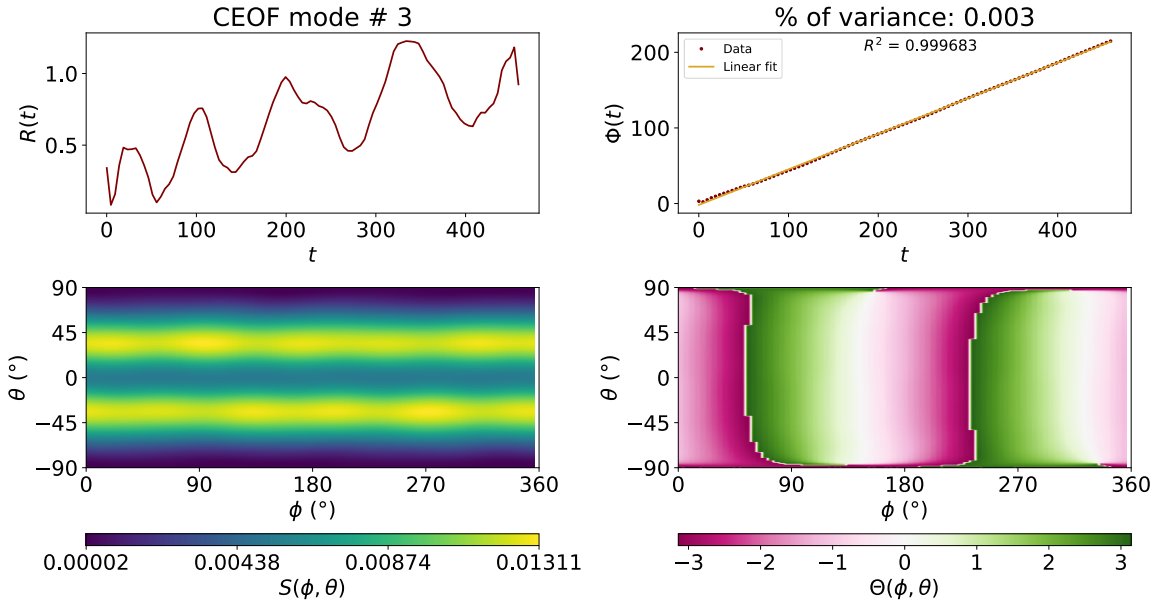

Figure 4.10: Third CEOF mode of h, corresponding to the wave with $\omega \sim 0.47$. The four measures defined by Equations (2.9)–(2.12) are plotted.

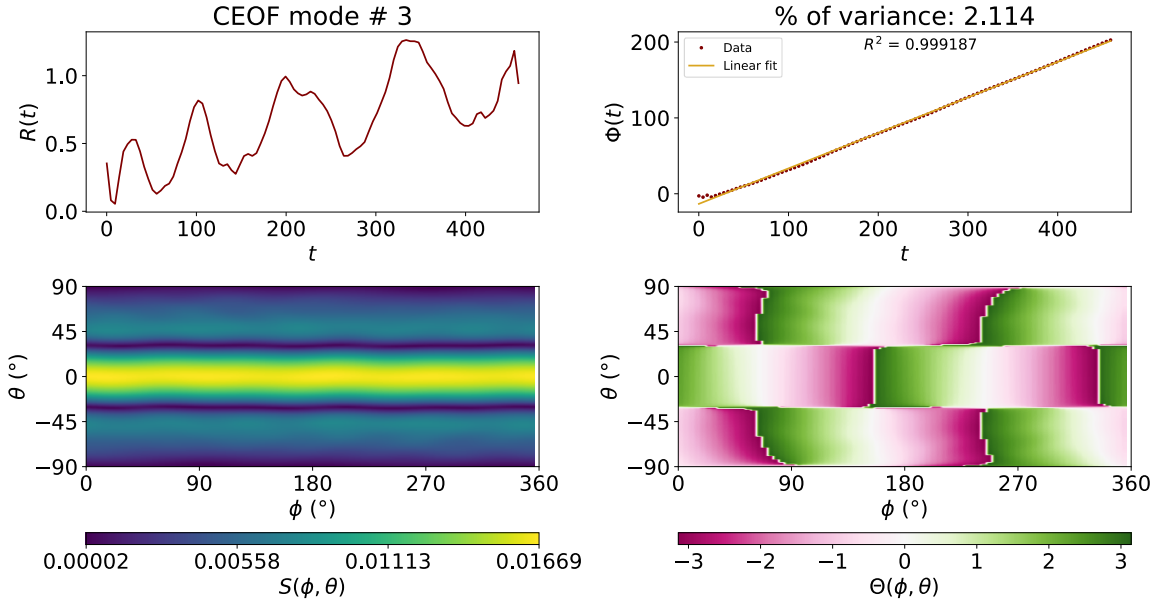

Figure 4.11: Third CEOF mode of u, corresponding to the wave with $\omega \sim 0.47$. The four measures defined by Equations (2.9)–(2.12) are plotted.

Let us start describing the general properties of the CEOF mode of h; see Figure 4.10. We see that it only accounts for 0.003% of variance of the field and despite of this its wave properties stand out very clearly. Its temporal phase has a linear dependence with t, it propagates in the azimuthal direction and is standing in the θ-direction. Its temporal amplitude shows an increasing trend superposed on several oscillations. Once more we hypothesise that this behaviour may be the result of this wave being involved in the exchange of kinetic and potential energy with the differential rotation. This would in turn cause the decrease of the temporal amplitude of the first CEOF modes of h and u. The spatial amplitude is such that h is zero at the equator and the poles and has a maximum at mid latitudes.

The variance of the CEOF modes of u and v are larger than that of h, reaching 19% in the

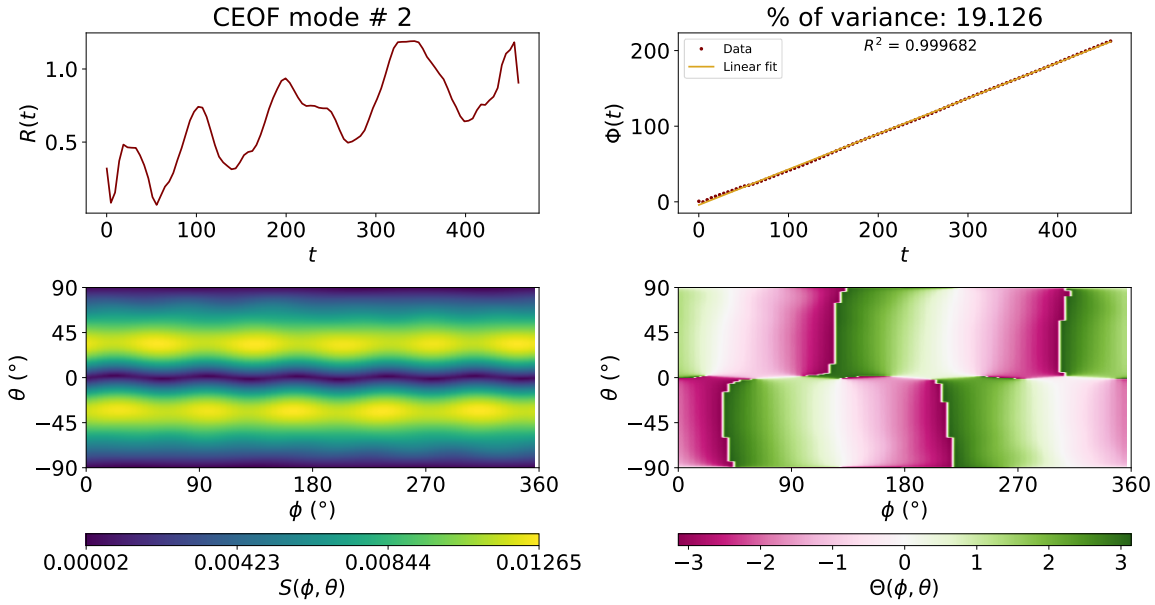

Figure 4.12: Second CEOF mode of v, corresponding to the wave with $\omega \sim 0.47$. The four measures defined by Equations (2.9)–(2.12) are plotted.

case of v. This trend of increasing variance when going from h to u and then to v is the same we found with the wave examined in Section 4.3.2. The temporal amplitudes of the three CEOF modes are quite similar. And the spatial amplitudes of h and v possess a similar latitudinal dependence and peak at $\theta \sim 40°$. As for the spatial amplitude, u is maximum at the equator and displays two smaller maxima at mid latitudes. None of these functions have maxima at the poles. Moreover, all three CEOF measures display clear signs of lack of azimuthal symmetry, with variations of one of the variables in this direction reaching up to 20% about the mean. Hence, the spatial properties of this wave differ from those of the wave with $\omega \sim 0.21$. Finally, it is time to analyse the wavenumbers. All three variables have two wavelengths in the longitudinal direction, hence $k_\phi \sim -2$ rad^{-1}, where the minus sign tells us that this wave also propagates in the direction opposite to rotation. Because of this wavelength, this wave is the first harmonic in the ϕ-direction. The behaviour of the three CEOF modes in the θ-direction is that of a standing wave, but now the latitudinal wavelengths of h and v are larger than those of the wave with $\omega \sim 0.21$. In fact, h is essentially independent of θ, that is, it only has half square wave. The non-uniform wavelength found in v in Figure 4.7 is not found in any of the present variables.

Animations of the three CEOF modes associated to the wave explored in this section are provided in this link. We now appreciate the propagation of waves with a non-constant amplitude that oscillates with an increasing trend. We also see the different spatial structure of the three eigenfunctions. But contrary to our finding of a negative k_ϕ, in these animations the wave is a prograde one. Although we have checked our plotting program, we have not been able to find the reason for this discrepancy in the direction of longitudinal wave propagation.

4.3.4 Wave with frequency near 0.22

Finally, the third CEOF mode of the latitudinal velocity component, v, contains only 0.565% of variance of the field. As we can see in the top left panel of Figure 4.13, the temporal amplitude oscillates between 0 and 0.2 and has a gradual decrease. Once again, the exchange of energy between waves and the differential rotation can be at the root of this behaviour. As usual, a least-squares linear fit to the temporal phase has been performed and the frequency and the Pearson R^2 coefficient have been determined. This time the linearity of $\Phi(t)$ is clearly not as good as before. Interestingly, the obtained frequency is very close to that of the first wave

(for the complete information about the present wave, see Table 4.1). The spatial amplitude shows a behaviour that we have not seen in previous CEOF modes. It has bands of maxima and minima, but azimuthal variations are also noticeable. There are no well defined patterns. The spatial phase displays an analogous behaviour. A longitudinal propagating character with $k_\phi \sim -1$ rad^{-1} can be guessed, together with several latitudinal bands reminiscent of a square wave. So both the frequency and k_ϕ are quite close to those of the first wave. Then, it is possible that the third CEOF mode of v is associated to a non-linear behaviour. In particular, maybe the wave of Section 4.3.2 is affected by non-linearity and the CEOF method has separated it in two parts: the CEOF modes of Section 4.3.2 and the current one. This agrees with the findings of Terradas et al. (2004), who obtained two CEOF modes of similar frequency when studying the intensity oscillations at the foot of a coronal loop. They interpreted that the non-stationarity of these oscillations led the CEOF method to separate them into two modes.

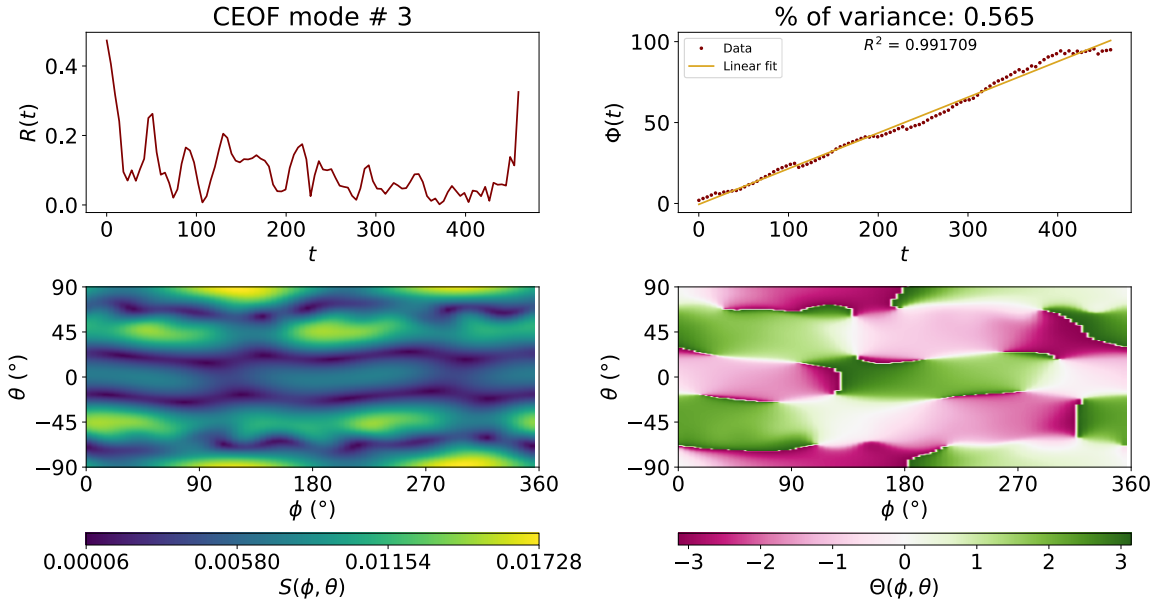

Figure 4.13: Third CEOF mode of v, corresponding to the wave with $\omega \sim 0.22$. The four measures defined by Equations (2.9)–(2.12) are plotted.

This time more than ever cuts along the latitudinal and longitudinal directions will help us. They are shown in Figure 4.13. The cut of $\Theta(\phi, \theta)$ along $\theta = N_\theta/2$ shows that we have propagation in the negative ϕ-direction. The linear fit done after the unwrap of $\Theta(\phi)$ provides us with the wavenumber k_ϕ. Also, note that the amplitude $S(\phi)$ is not constant and does not reach zero, which can be a consequence of non-linearity. In addition, $S(\theta)$ shows three different amplitudes and there is no vertical symmetry in none of them. $\Theta(\theta)$ is not a sawtooth function and vaguely reminds us of a square function: we can "feel" the presence of two different plateaus separated by $\sim \pi$.

An animation of the CEOF mode of v can be found in this link. It presents retrograde propagation with a varying amplitude and a long wavelength in the ϕ-direction.

4.4 Conclusions

The analysis of the numerical simulation performed in this chapter proves that the CEOF method can provide information about waves even in the non-linear regime. We have been able to characterise in detail the two lowest-frequency Rossby waves. The frequency, the character (propagating and standing in the ϕ- and θ-directions, respectively) and the temporal and spatial dependence of the variables h, u and v, including the wavenumbers k_ϕ and k_θ, have been

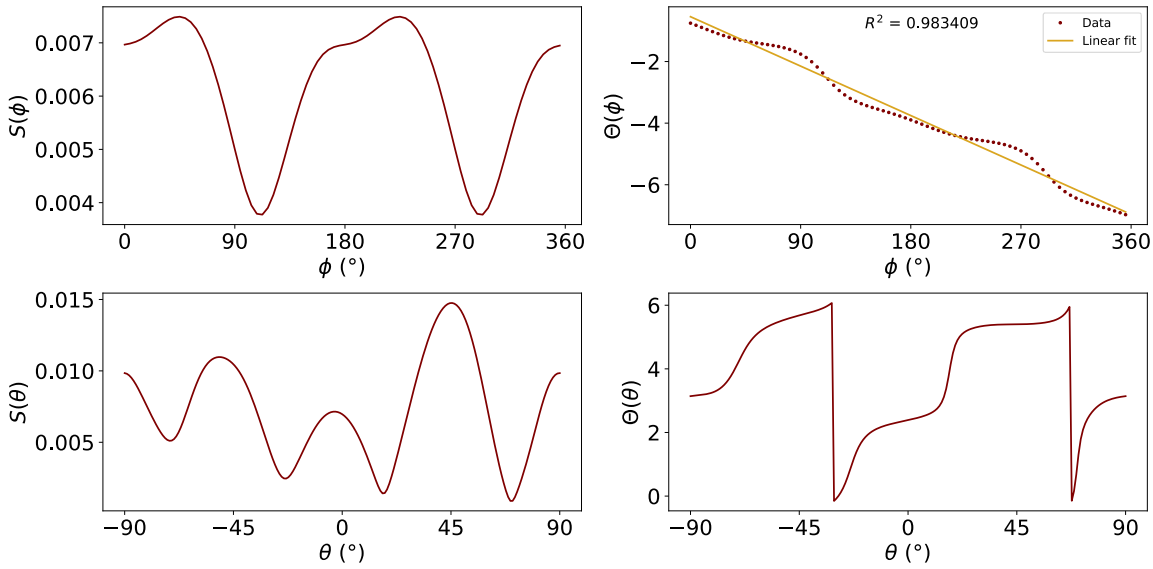

Figure 4.14: Cuts of the third CEOF mode of v, shown in Figure 4.13. The two CEOF spatial measures defined by Equations (2.9) and (2.10) are plotted for $\theta = N_\theta/2$ and $\phi = N_\phi/2$ in the top and bottom panels, respectively.

obtained.

We have been more concerned with the applicability of the CEOF analysis to the present problem than to explore the physical implications of the results. The possible extensions to this chapter are discussed in Section 5.2.

Chapter 5

Discussion and future work

5.1 Discussion

In this thesis we have used the CEOF analysis introduced by Barnett (1983) to extract the parameters of both standing and propagating waves contained in a scalar field. After presenting the method, following the idea of Terradas et al. (2004), we have tested it with one- and two-dimensional synthetic signals made of the sum of several waves. In the one-dimensional case we have added a propagating and a standing wave. The result of the CEOF analysis has helped us to explain the interpretation of the CEOF functions. Also, the parameters of both waves have been recovered with outstanding accuracy. We have concluded that the temporal phase, given by Equation (2.12), has to be linear with time if we have a physical mode of oscillation. The slope of the linear least-squares fit provides the frequency of the wave, ω. To have a linear behaviour we have unwrapped the sawtooth functions by adding or removing 2π in the phase jump. The spatial phase, Equation (2.10), has to be linear with space or be a square function to have a propagating or a standing wave, respectively. In both cases, $\Theta(\vec{r}_k)$ is related with the wavenumber, k. The temporal amplitude, Equation (2.11), except for edge effects, tends to a constant value. And finally, the spatial amplitude, Equation (2.9), is constant (or equal to the absolute value of a cosine) if the wave is propagating (standing). The amplitude of a wave can be recovered as the product of the average of $R(t)$ times the average (the maximum) of $S(\vec{r}_k)$ for a propagating (standing) wave.

This information has been very useful to analyse the two-dimensional field. It consisted in the sum of a wave that propagates in the two directions, a standing wave in the two directions and a wave that propagates in one direction and is standing one in the other. Adding one dimension leads to an increase in the complexity of the analysis. However, the CEOF method has identified the wave features of each component and we have noticed that the main parameter that affects the contribution to the variance of the field is the wave amplitude. Once again, the amplitude, frequency and wavenumbers have been extracted with extraordinary accuracy. In this case, taking cuts along fixed locations has helped the interpretation of the spatial measures. This way we could compare both one- and two-dimensional tests to find similar behaviours.

To finish with our tests, we have studied how noise affects the CEOF method by adding white noise to our two-dimensional field, given by Equation (3.10). Adding noise to our test signal has not prevented the CEOF method from identifying each wave and again their parameters have been properly recovered.

Finally, we have applied the CEOF method to a numerical simulation of the tachocline (Dikpati (2012) and Dikpati et al. (2017)). The hydrodynamics of the tachocline is described in terms of three different dependent variables: the perturbation of tachocline thickness, h, and the longitudinal and latitudinal velocity components, u and v. The CEOF method has been applied to each variable with the purpose of finding physical modes of oscillation. With the CEOF analysis, we have extracted two CEOF modes of h and u that correspond to the tachocline

differential rotation. Furthermore, we have been able to obtain the wave parameters of two wave modes present in the three variables with frequencies near 0.21 and 0.47. The decreasing or increasing behaviour of the temporal amplitude suggests that there may be exchange of energy between the tachocline differential rotation and the physical modes of oscillation. Keeping in mind that this simulation starts with a certain initial condition, to more accurately analyse these changes in amplitude it would be necessary to reach the steady state. Nevertheless, a non-constant amplitude is probably an evidence of the presence non-linear waves in the two-dimensional fields.

In one sentence, the summary is that the potential of the CEOF method is shown in this work: it is able to separate with an extraordinary accuracy linear waves and also notice the presence of non-linear waves in the field.

5.2 Future work

Both in the test cases and in the tachocline numerical simulation results, it is necessary to perform a careful estimation of the errors of the amplitude, frequency and wavenumbers. The results presented in Tables 3.1, 3.2, 3.3 and 4.1 contain two or three decimal figures but we have not ensured that they are the relevant ones. The error of a quantity that is obtained from a least-squares fit is easy to estimate. This applies to the wave frequency and the wavenumber of a propagating wave, but also to the spatial amplitude of a standing wave: in some cases this amplitude can be approximated by the absolute value of sinusoidal function. The amplitude of $R(t)$ is equal to its mean once we remove the initial and final times for which edge effects are dominant. Hence, the uncertainty of $R(t)$ can be estimated as its standard deviation. Finally, the wavelength of a standing wave comes from the distance spanned by the square waves present in the domain divided by the number of such waves. The corresponding error can be difficult to estimate, especially with a phase such as $\Theta(\theta)$ of Figure 4.14.

It is possible to apply the CEOF analysis to a data cube made by joining the three cubes of h, u and v by one of their sides. The three cubes combined would have a size of either $3N_\phi \times N_\theta \times N_t$ or $N_\phi \times 3N_\theta \times N_t$, depending on whether they are attached at one of their $\phi = \text{const}$ or $\theta = \text{const}$ sides, respectively. This has the advantage that the CEOF modes of h, u and v that we obtained independently in Sections 4.3.2 and 4.3.3 are represented by a single CEOF mode with a one function $R(t)$, one function $\Phi(t)$ and three paris of spatial functions $S(\phi, \theta)$ and $\Theta(\phi, \theta)$, one for each of the physical variables.

A physical application of the results of Chapter 4 is also in order. The spatial profiles of the physical variables associated to each wave can be compared with the profiles of Dikpati (2012). The problem is that we are not aware that the Rossby wave frequency and eigenfunctions have been computed before for the differential rotation profile used by Dikpati (2012). Another physical application is to compute the kinetic and potential energy of the waves of Sections 4.3.2 and 4.3.3 and to study their possible role in the energy interchange described by Dikpati (2012) and Dikpati et al. (2017). This way we could answer the question of whether the energy interchange between the tachocline differential rotation and Rossby waves can be ascribed to particular wave modes.

Another interesting issue is our finding of four frequencies that are present in the tachocline hydrodynamic simulation; see Figure 4.2. Two of these frequencies ($\omega \sim 0.21$ and $\omega \sim 0.47$) have been later retrieved in the CEOF analysis of the data sets. But what happens with the other two? The frequency $\omega \sim 0.08$, present in h only, may be restricted to specific latitudinal bands and for this reason it escaped detection with the CEOF method. It would then be interesting to study its distribution in a (ϕ, θ) map. Then, the CEOF analysis could be performed in the corresponding restricted spatial domain. As shown by Figure 4.2, the other frequency, $\omega \sim 0.42$, is quite common and so its absence in the CEOF results is a bit of a mystery. It deserves special attention and perhaps the (ϕ, θ) maps of h, u and v could shed some light on its nature.

Bibliography

Anderson, J. R. 1982, Master's thesis, Dept. Meteor. Phys. Oceanogr., MIT, 77 p.

Barnett, T. P. 1983, Monthly Weather Review, 111, 756

Charbonneau, P. 2020, Living Reviews in Solar Physics, 17, 4

Dikpati, M. 2012, The Astrophysical Journal, 745, 128

Dikpati, M., Cally, P. S., McIntosh, S. W., & Heifetz, E. 2017, Scientific Reports, 7, 14750

Dikpati, M. & Gilman, P. A. 2001, The Astrophysical Journal, 551, 536

Rasmusson, E. M., Arkin, P. A., Chen, W.-Y., & Jalickee, J. B. 1981, Monthly Weather Review, 109, 587

Terradas, J., Oliver, R., & Ballester, J. L. 2004, The Astrophysical Journal, 614, 435

VanderPlas, J. T. 2018, The Astrophysical Journal Supplement Series, 236, 16

Wallace, J. M. & Dickinson, R. E. 1972, Journal of Applied Meteorology, 11, 887